AFRL-AFOSR-JP-TR-2024-0014

Bio-Inspired Compliant Musculoskeletal Actuation for Wings and Fins of Miniature Robotic Systems

Ravi, Sridhar
University of New South Wales-NEW NCAGE Code
HIGH STREET
KENSINGTON, NSW, ,
AU

12/11/2023
Final Technical Report

Air Force Research Laboratory
Air Force Office of Scientific Research
Asian Office of Aerospace Research and Development
Unit 45002, APO AP 96338-5002

REPORT DOCUMENTATION PAGE

PLEASE DO NOT RETURN YOUR FORM TO THE ABOVE ORGANIZATION.

1. REPORT DATE	2. REPORT TYPE	3. DATES COVERED	
20231211	Final	START DATE 20190927	END DATE 20210926

4. TITLE AND SUBTITLE
Bio-Inspired Compliant Musculoskeletal Actuation for Wings and Fins of Miniature Robotic Systems

5a. CONTRACT NUMBER	5b. GRANT NUMBER	5c. PROGRAM ELEMENT NUMBER
	FA2386-19-1-4066	
5d. PROJECT NUMBER	**5e. TASK NUMBER**	**5f. WORK UNIT NUMBER**

6. AUTHOR(S)
Sridhar Ravi

7. PERFORMING ORGANIZATION NAME(S) AND ADDRESS(ES)
University of New South Wales-NEW NCAGE Code
HIGH STREET
KENSINGTON, NSW
AU

8. PERFORMING ORGANIZATION REPORT NUMBER

9. SPONSORING/MONITORING AGENCY NAME(S) AND ADDRESS(ES)	10. SPONSOR/MONITOR'S ACRONYM(S)	11. SPONSOR/MONITOR'S REPORT NUMBER(S)
AOARD UNIT 45002 APO AP 96338-5002	AFRL/AFOSR IOA	AFRL-AFOSR-JP-TR-2024-0014

12. DISTRIBUTION/AVAILABILITY STATEMENT
A Distribution Unlimited: PB Public Release

13. SUPPLEMENTARY NOTES

14. ABSTRACT
Insects are spectacular flyers and display exceptional maneuverability made possible through nimble wing actuation and articulation. Recent research has revealed that the kinematics of the flapping wing in insects is not fully governed by active control and instead passive dynamics play an important role on the overall performance. This project focused on seeking to understand the effects of passive pitch dynamics on the kinematics and performance of flapping wings through a combination of experimental and numerical means. In chapter 2 we report on a high-fidelity numerical framework developed to study passively pitching flapping wings using an immersed boundary-lattice Boltzmann method (IB-LBM). In this chapter we also discuss the results from our investigation of passively pitching of tandem rectangular wings in free hovering condition. As insect wings vary widely in shape, in Chapter 3 we present results on a parametric study performed to investigate the effects of wing shape and structural properties of the hinge on aerodynamics performance. Finally in Chapter 4, the results from an experimental study on the effects of external fluid mechanic perturbations on the performance of passively pitching wings at low Reynolds numbers is presented.

15. SUBJECT TERMS

16. SECURITY CLASSIFICATION OF:			17. LIMITATION OF ABSTRACT	18. NUMBER OF PAGES
a. REPORT	b. ABSTRACT	c. THIS PAGE		
U	U	U	SAR	53

19a. NAME OF RESPONSIBLE PERSON	19b. PHONE NUMBER *(Include area code)*
FUMIO KOJIMA	315-227-7007

Standard Form 298 (Rev.5/2020)
Prescribed by ANSI Std. Z39.18

Compliant Musculoskeletal Actuation in Flying Insects and Bio-inspired Designs for Miniature Robots

Grant Number: FA2386-19-1-4066

Name and Position/Title of Principle Investigator:
Dr Sridhar Ravi, Senior Lecturer, UNSW-Canberra

Key Researcher(s) involved in the Proposed Project:
Professor Matthew Garratt, UNSW-Canberra
Dr Fangbao Tian, Senior Lecturer, UNSW-Canberra
Dr Soudeh Mazharmanesh, Research Associate, UNSW-Canberra
Dr Qiuxiang Huang, Research Associate, UNSW-Canberra

Proposed Period-of-Performance: 27 Sep 19 - 26 Sep 21
Proposed Total Cost (for each year): Year 1: 78.3k, Year 2: 80k

Contents

1 Abstract

Insects are spectacular flyers and display exceptional maneuverability made possible through nimble wing actuation and articulation. Recent research has revealed that the kinematics of the flapping wing in insects is not fully governed by active control and instead passive dynamics play an important role on the overall performance. This project focused on seeking to understand the effects of passive pitch dynamics on the kinematics and performance of flapping wings through a combination of experimental and numerical means. In chapter 2 we report on a high-fidelity numerical framework developed to study passively pitching flapping wings using an immersed boundary-lattice Boltzmann method (IB-LBM). In this chapter we also discuss the results from our investigation of passively pitching of tandem rectangular wings in free hovering condition. As insect wings vary widely in shape, in Chapter 3 we present results on a parametric study performed to investigate the effects of wing shape and structural properties of the hinge on aerodynamics performance. Finally in Chapter 4, the results from an experimental study on the effects of external fluid mechanic perturbations on the performance of passively pitching wings at low Reynolds numbers is presented.

2 High efficiency and high-fidelity immersed boundary-lattice Boltzmann method numerical simulation framework for flapping wings

2.1 Introduction

Many insects have spring-like elements in the form of elastic materials in their thoraxes, muscles, and tendons that may reduce the energetic demands of flapping flight and improve flight efficiency (Lynch et al., 2021). During the flapping flight, insects apply their muscle forces through the axis close to the leading edge, which creates a moment with respect to the mass centre of the wing, leading to the passive pitching of the wing due to the interaction between the wing and the surrounding airflow (Ennos, 1988b). Inspired by insect flight, passively pitching flapping wings have been implemented in micro aerial vehicles (MAVs) designs (Farrell Helbling and Wood, 2018). In order to understand the passive pitching mechanism of flapping wings, various experimental and numerical studies have been conducted (Mazharmanesh et al., 2021; Lei and Li, 2020). However, passive pitching of tandem ipsilateral wings (e.g. dragonfly) has not been fully explored. Here, the computation of a rigid rectangular flapping plate with prescribed flapping and pitching motions and a rigid fruit fly wing with passive pitching in hovering flight are conducted to validate the present immersed boundary-lattice Boltzmann method (IB-LBM) solver. The validated solver is then applied to simulate the passive pitching of tandem rectangular and dragonfly wings.

2.2 Model description

The unsteady incompressible flow is governed by the continuity and Navier-Stokes equations

$$\nabla \cdot \boldsymbol{u} = 0, \quad \frac{\partial \boldsymbol{u}}{\partial t} + \boldsymbol{u} \cdot \nabla \boldsymbol{u} = -\frac{1}{\rho}\nabla p + \nu \nabla^2 \boldsymbol{u} + \boldsymbol{f}, \tag{1}$$

where $\boldsymbol{u}$ is the fluid velocity, ρ is the constant density, $\boldsymbol{f}$ is the body force and p and ν are pressure and kinematic viscosity, respectively.

2.3 CFD solver validation

The D3Q19 lattice Boltzmann method (LBM) with multi-relaxation-time (MRT) model is adopted for simulation of the fluid dynamics. The two-way fluid-structure interactions are coupled by a feedback immersed boundary method (IBM). In the LBM, the computational domain is discretised with a fixed Eulerian grid (lattice grid). The fluid is modelled as a set of fictive particles undergoing streaming and collision over a lattice grid. The macroscopic dynamics of the fluid is the result of the statistical behaviour of the particles, which are described by the distribution function $g_i(\boldsymbol{x}, t)$. The evolution of this distribution function is according to (Lallemand and Luo, 2000; Luo et al., 2011)

$$g_i(\boldsymbol{x} + \boldsymbol{e}_i \Delta t, t + \Delta t) - g_i(\boldsymbol{x}, t) = \Omega_i(\boldsymbol{x}, t) + \Delta t G_i, \tag{2}$$

where $g_i(\boldsymbol{x}, t)$ is the distribution function for particles with velocity $\boldsymbol{e}_i$ at position $\boldsymbol{x}$ and time t, Δt is the time increment, $\Omega_i(\boldsymbol{x}, t)$ is the collision operator and G_i is the forcing term

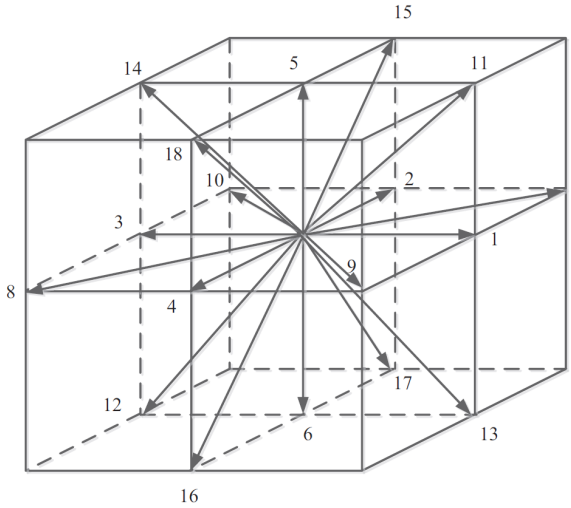

Figure 1: Lattice arrangement for D3Q19 model. "D3" stands for "3 dimensions", while "Q19" stands for "19 particle speeds". The zero velocity $\boldsymbol{e_0}$ is not shown.

accounting for the body force $\boldsymbol{f}$. The D3Q19 model (D'Humieres et al., 2002) is used on a cube lattice. The lattice arrangement for D3Q19 model is shown in figure 1.

There are several methods to handle the collision operator $\Omega_i(\boldsymbol{x}, t)$, such as single-relaxation-time (SRT) model, two-relaxation-time (TRT) model and multiple-relaxation-time (MRT) model (Krüger et al., 2017). Compared to the SRT collision model, the MRT collision model has been proven to be more numerically stable (Lallemand and Luo, 2000; Luo et al., 2011) and therefore is adopted in the current research. In the MRT collision model, the collision operator is given by (Lallemand and Luo, 2000; D'Humieres et al., 2002):

$$\Omega_i = -(\boldsymbol{M}^{-1}\boldsymbol{S}\boldsymbol{M})_{ij}[g_i(\boldsymbol{x}, t) - g_i^{eq}(\boldsymbol{x}, t)], \tag{3}$$

where $\boldsymbol{M}$ is a 19×19 transform matrix for D3Q19 model and $\boldsymbol{S} = diag(\tau_0, \tau_1, \ldots, \tau_{18})^{-1}$ is a non-negative diagonal relaxation matrix. The determination of $\boldsymbol{S}$ in three-dimensional model can be found in D'Humieres et al. (2002). The equilibrium distribution function g_i^{eq} is defined as

$$g_i^{eq} = \rho\omega_i\Big[1 + \frac{\boldsymbol{e_i}\cdot\boldsymbol{u}}{c_s^2} + \frac{\boldsymbol{uu} : (\boldsymbol{e_i e_i} - c_s^2\boldsymbol{I})}{2c_s^4}\Big], \tag{4}$$

where $c_s = \Delta x/(\sqrt{3}\Delta t)$ is the speed of sound, Δx is the lattice spacing, $\boldsymbol{I}$ is the unit tensor and the weighting factors ω_i are given by $\omega_0 = 1/3$, $\omega_{1-6} = 1/18$ and $\omega_{7-18} = 1/36$. The velocity $\boldsymbol{u}$, mass density ρ and pressure p can be obtained according to

$$\rho = \sum_i g_i, \quad p = \rho c_s^2, \quad \boldsymbol{u} = (\sum_i \mathbf{e}_i g_i + \frac{1}{2}\boldsymbol{f}\Delta t)/\rho, \tag{5}$$

The force scheme proposed in Guo et al. (2002) is adopted to determine G_i,

$$G_i = [\boldsymbol{M}^{-1}(\boldsymbol{I} - \boldsymbol{S}/2)\boldsymbol{M}]_{ij}F_i, \tag{6}$$

$$F_i = \Big(1 - \frac{1}{2\tau}\Big)\omega_i\Big[\frac{\boldsymbol{e}_i - \boldsymbol{u}}{c_s^2} + \frac{\boldsymbol{e}\cdot\boldsymbol{u}}{c_s^4}\boldsymbol{e}_i\Big]\cdot\boldsymbol{f}, \tag{7}$$

where τ is the non-dimensional relaxation time.

In the present study a feedback IBM (Huang et al., 2021a) is adopted to handle the no-slip boundary conditions on the flapping wing. In this method a body force $\boldsymbol{f}$ is added in the Navier-Stokes equation to mimic a boundary condition according to

$$\boldsymbol{f}(\boldsymbol{x},t) = -\int \boldsymbol{F}_{ib}(s,t)\delta(\boldsymbol{x}-\boldsymbol{X}(s,t))dA, \tag{8}$$

$$\boldsymbol{F}_{ib}(s,t) = \alpha\rho(\boldsymbol{x},t)(\boldsymbol{U}_{ib}(s,t)-\boldsymbol{U}(s,t)), \tag{9}$$

$$\boldsymbol{U}_{ib}(s,t) = \int \boldsymbol{u}(x,t)\delta(\boldsymbol{x}-\boldsymbol{X}(s,t))d\boldsymbol{x}, \tag{10}$$

where $\boldsymbol{F}_{ib}(s,t)$ is the Lagrangian force density, dA is the element surface area of the immersed boundary, $\delta(\boldsymbol{x}-\boldsymbol{X}(s,t))$ is Dirac's delta function, $\boldsymbol{x}$ is the coordinate of the fluid lattice nodes, $\boldsymbol{X}$ is the coordinate of the structure (i.e. the flapping wing here), α is the feedback coefficient and $\alpha = 2s$ in LBM simulations. In dimensionless form $\alpha^* = \alpha/(U_{ref}/L_{ref}) = 40$, and α^* ranges from 20 to 104 (Huang et al., 2021a). Here U_{ref} and L_{ref} are the reference velocity and length, respectively. $\boldsymbol{U}_{ib}(s,t)$ is the immersed boundary velocity obtained by interpolation at the immersed boundary and $\boldsymbol{U}(s,t)$ is the velocity of the wing. The 4-point discrete delta function $\delta_h(\boldsymbol{x})$ is used to approximate the Dirac delta function Peskin (2002),

$$\delta_h(\boldsymbol{x}) = \frac{1}{\Delta x\Delta y\Delta z}\zeta(\frac{x}{\Delta x})\zeta(\frac{y}{\Delta y})\zeta(\frac{z}{\Delta z}), \tag{11}$$

$$\zeta(r) = \frac{1}{8}\left(3-2|r|+\sqrt{1+4|r|-4r^2}\right) \quad 0\le|r|\le 1, \tag{12}$$

$$\frac{1}{8}\left(5-2|r|+\sqrt{-7+12|r|-4r^2}\right) \quad 1\le|r|\le 2, \tag{13}$$

$$0 \qquad |r|>2. \tag{14}$$

The numerical method used here has been extensively validated and applied in confined flows (e.g. 2D collapsible channel flows and 3D collapsible tube flows) in our previous publications (Huang et al., 2020a, 2021a,b). Here the simulations of a rectangular flapping wing and a fruit fly flapping wing are further considered to validate the computations of 3D flapping wings. To reduce the computational effort, a multi-block LBM (Yu et al., 2002) is adopted to provide high resolution near the solid body, with low resolution in the farfield. A hybrid open multi-processing (OpenMP) and message passing interface (OpenMPI) parallel computing strategy has been incorporated into the code to accelerate the computation.

2.3.1 A rigid rectangular flapping plate with prescribed flapping and pitching motions

A thin and rigid rectangular plate in hovering flight with prescribed flapping and pitching motions is considered, as shown in figure 2. The wing has a chord length c and a span of $L = 2c$. The aspect ratio is $AR = L/c = 2.0$. The leading edge undergoes two degrees-of-freedom rotations as the torques activate the wing at the pivot point (Dai et al., 2012),

$$\phi = \frac{A_\phi}{2}\sin\left(2\pi ft+\frac{\pi}{2}\right), \quad \theta = \frac{A_\theta}{2}\sin(2\pi ft), \tag{15}$$

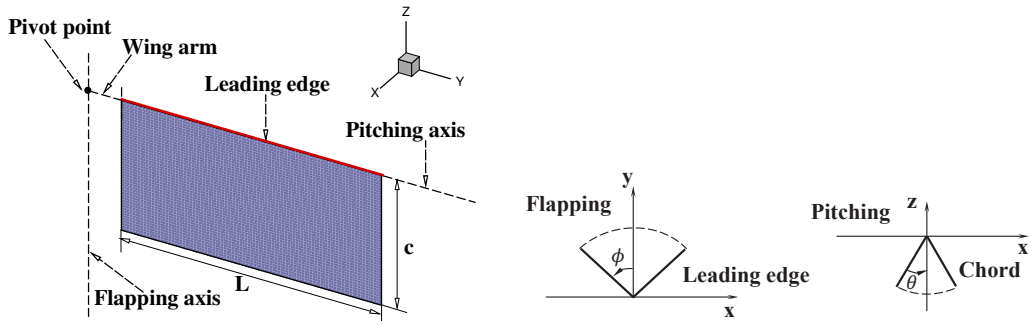

(a) 3D view (b) 2D view

Figure 2: Schematic diagram of the rectangular wing model used in the study.

Table 1: Fluid domain size in $x-$, $y-$, and $z-$ directions, finest grid size, grid number, and CPU time t_w of one stroke cycle for the computation of the rectangular wing model. h: hour.

Sources	Domain size	Finest grid size	Grid number (10^6)	$t_w(h)$/ cycle
Dai et al. (2012)	[14c, 15c, 15c]	0.05c	1.72	14
Present IB-LBM	[14c, 15c, 15c]	0.05c	3.14	0.18

where ϕ is the flapping angle, θ is the pitching angle, f is the flapping frequency, and $A_\phi = 2\pi/3$ and $A_\theta = \pi/3$ are the flapping and pitching amplitudes, respectively. The wing arm (from the pivot point to the wing root) has length $0.1c$. The Reynolds number, drag and lift coefficients are defined as

$$\mathrm{Re} = \frac{Uc}{\nu} = 176, \quad C_D = \frac{2F_x}{\rho U^2 A}, \quad C_L = \frac{2F_z}{\rho U^2 A}, \tag{16}$$

where U is the mean wingtip velocity at the leading edge and $U = 2A_\phi f(L + 0.1c) = 8.797cf$. Here F_x and F_z are the force acting on the wing by the ambient fluid in x and z direction, respectively. A is the surface area of the wing ($A = cL$ for a rectangular plate). As shown in table 1, the rectangular computational domain has a size of $14c \times 15c \times 15c$, which is the same size as that of Dai et al. (2012). The most refined grid around the wing is $0.05c$, and the total grid number is 3.14×10^6. The CPU time per one stroke cycle of the present IB-LBM solver is almost two orders of magnitude lower than that in Dai et al. (2012). Five stroke cycles are simulated to ensure that all the force histories (e.g. C_D and C_L) have reached steady state. Dirichlet boundary conditions for the velocity and pressure are applied on all six computational boundaries. The grid size of the wing is maintained at half of the fluid grid size. Figure 3(a) shows the wing kinematics, where the flapping motion leads the pitching motion by a phase of 90^o. A grid convergence study was performed where the grid size (dx) was systematically decreased from 0.1c to 0.025c. Figure 3(b) shows the comparison of lift coefficient C_L in three different grids densities. The variation in C_L was consistent across the last two consecutive cycles for all three grid sizes, indicating that the flow field had reached a periodic state. The converged solution for C_L produced by $dx = 0.025c$ agrees well with the computational result of Dai et al. (2012).

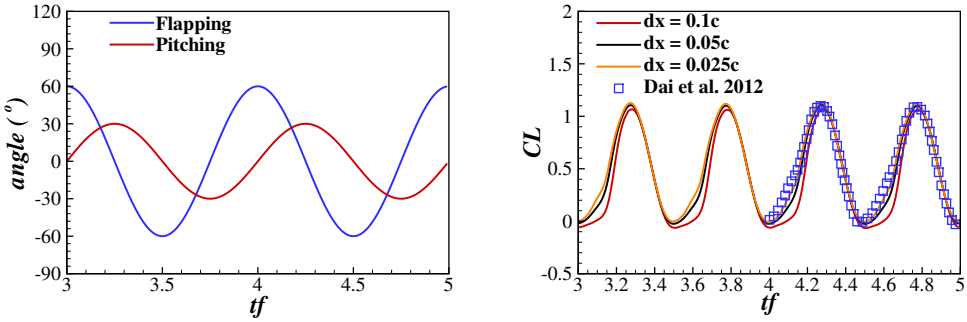

(a) Wing kinematics (b) C_L

Figure 3: Rectangular wing: wing kinematics in two stroke cycles and the time history of the lift coefficient.

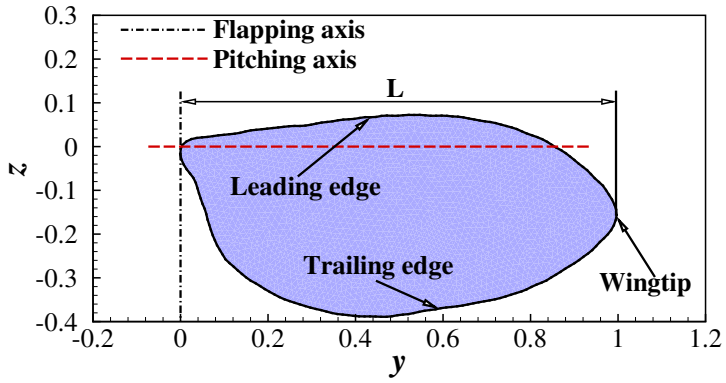

Figure 4: Shape and dimensions of the fruit fly wing model.

2.3.2 A rigid fruit fly plate with passive pitching in hovering flight

A fruit fly wing in hovering flight with passive pitching is considered to further validate the current solver. Figure 4 shows the shape and dimensions of the wing. The passive pitching mechanism is numerically modelled by a torsional spring. The wing has a mean chord length c with an aspect ratio $AR = L^2/A = 3.2$, where L is the wingspan and A is the wing surface area. The kinematics of the wing are defined as a combination of the prescribed rotation around $z-$axis and the passive pitching motion around $y-$axis.

$$\phi(t) = -\frac{A_\phi}{2}\cos(2\pi f t), \tag{17}$$

where $A_\phi = 7\pi/9$ is the flapping amplitude and f is the flapping frequency. In the numerical simulation, the pitching angle θ is determined by solving the equation of passive feathering motion of the wing, as described in Kolomenskiy et al. (2019),

$$J_{yy}\ddot{\theta}(t) + C\dot{\theta}(t) + K_s\left(\theta(t) - \theta_0\right) = M_{\text{aero}} + J_{zy}\ddot{\phi}(t)\cos\theta(t) + \frac{1}{2}J_{yy}\dot{\phi}(t)^2\sin 2\theta(t), \tag{18}$$

where J_{yy} is the moment of inertia around $y-$axis (i.e. pitching axis) when the wing is rotated around $y-$axis, J_{zy} is the moment of inertia around $y-$axis when the wing is rotated around

Table 2: Fluid domain size in $x-$, $y-$, and $z-$ directions, finest grid size, grid number, and CPU time t_w of one stroke cycle for the computation of the fruit fly wing model. h: hour.

Sources	Domain size	Finest grid size	Grid number (10^6)	$t_w(h)$/ cycle
Lei and Li (2020)	[30c, 30c, 30c]	0.03c	6.99	–
Present IB-LBM	[30c, 30c, 30c]	0.03c	12.8	2.11

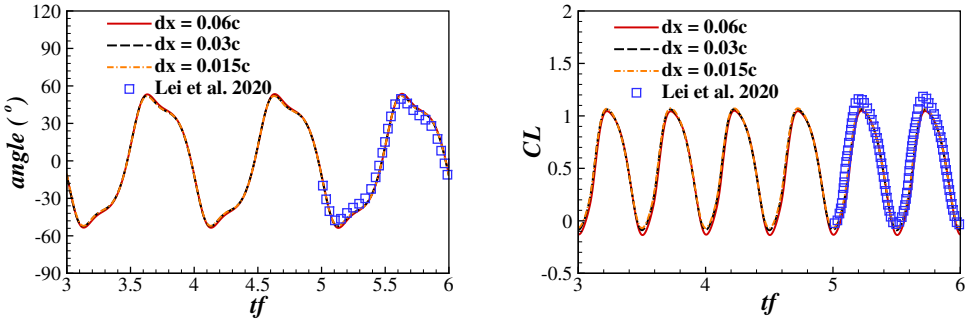

(a) Wing kinematics (b) C_L

Figure 5: Fruit fly wing: wing kinematics and the time history of the lift coefficient in three different grid sizes.

$z-$axis (i.e. flapping axis), $C = 0$ is the damping coefficient of the spring, K_s is the torsional stiffness of the spring, $\theta_0 = 0$ is the rest angle and M_{aero} is the aerodynamic pitching moment on the wing. The non-dimensional groups of the problem include the Reynolds number, mass ratio and the Cauchy number (a ratio between the aerodynamic force and the elastic spring force), which are respectively given by

$$Re = \frac{UL}{\nu} = 300, \quad M = \frac{\rho_w h}{\rho c} = 1, \quad Ch = \frac{\rho A_\phi^2 f^2 c^3 L^2}{K_s} = 0.15, \tag{19}$$

where $U = 2fA_\phi L$ is the mean wingtip velocity, ρ_w is the density of the wing and $h = 0.03c$ is the wing thickness. Table 2 shows the rectangular computational domain that has a size of $30c \times 30c \times 30c$, same as that used in Lei and Li (2020). The finest grid around the wing is $0.03c$, and the total grid number is 12.8×10^6. Six stroke cycles were simulated to ensure that the flow field reached a periodic state. Figure 5(a) shows the time history of the pitching angle, which agrees well with the computational result of Lei and Li (2020). The grid refinement study here shows that the solutions are converged.

2.3.3 Passively pitching tandem wings

Here hovering flight of tandem rectangular wings with passive pitching is simulated. Figure 6 shows the geometric parameters of the wings that have an aspect ratio of $AR = L/c = 3.0$. The flapping motions are prescribed as

$$Forewing: \quad \phi_f = \frac{\phi_{f0}}{2}\cos(2\pi ft) \quad Hindwing: \quad \phi_h = \frac{\phi_{f0}}{2}\cos(2\pi ft + \psi), \tag{20}$$

Table 3: Fluid domain size in $x-$, $y-$, and $z-$ directions, finest grid size, grid number, and CPU time t_w of one stroke cycle for the computation of the tandem flapping wing model. h: hour.

Sources	Domain size	Finest grid size	Grid number (10^6)	$t_w(h)$/ cycle
Present IB-LBM	[30c, 30c, 30c]	0.04c	9.21	0.63

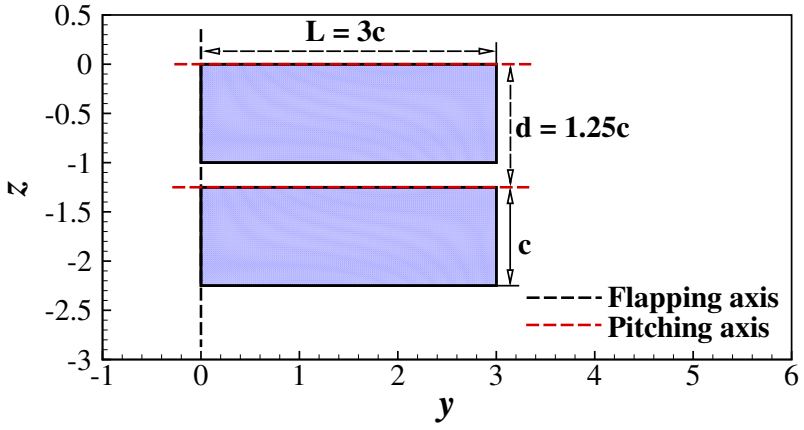

Figure 6: Geometric parameters of the tandem rectangular wings.

where ϕ_f and ϕ_h are the flapping angle for the forewing and hindwing, respectively. Here $\phi_{f0} = 80^o$ is the flapping amplitude and $\psi = \pi$ is the phase angle between the flapping motion of the wings. The pitching motion is solved by equation 18 where the spring damping $C = 0$ and wing thickness $h = 0.03c$. The Reynolds number $Re = UL/\nu = 300$, the Cauchy number $Ch = 0.15$ and mass ratio $M = 1$ were assumed for both wings. The distance between fore and hind wing $d = 1.25c$, which nominally matched that of real dragonflies. A rectangular computational domain of size of $30c \times 30c \times 30c$ was used and the finest grid around the wing was $0.04c$, and the total grid number was 9.21×10^6. Six stroke cycles were simulated. Table 3 shows the domain size and grid data used in this study. Six stroke cycles are simulated and the last cycle is used to data analysis. Figure 7(a) shows the forewing kinematics. The time history of the lift coefficient is shown in figure 7(b). The grid refinement study here shows the results are grid independent. Figure 8 shows the vortical structures at $tf = 5.7$, and the hingwing interacts with the shed vorties from the forewing is observed.

2.4 Passively pitching tandem dragonfly wings

Here hovering flight of tandem dragonfly wings with passive pitching is simulated. Figure 9 shows the geometric parameters of the wings. The wing shape belongs to the species *Aeshna Juncea*, chosen from Norberg (1972). The forewing is more slender in shape, while the hindwing is more broader near the base and marginally shorter than the forewing. The forewing has a mean chord of $c_f = 8mm$ and a span of $L_f = 49mm$, and the hindwing has a mean chord of $c_h = 11mm$ and a span of $L_h = 46mm$. The wing distance is $d = 1.25c = 10mm$, measured

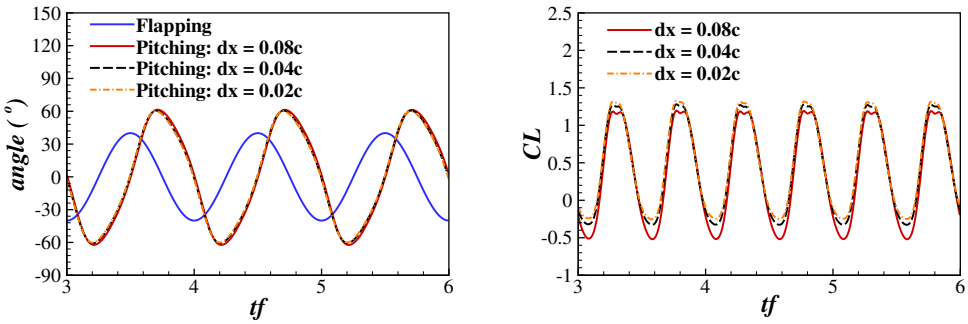

(a) Wing kinematics (b) C_L

Figure 7: Wing kinematics and the time history of the lift coefficient for the forewing in three different grid sizes.

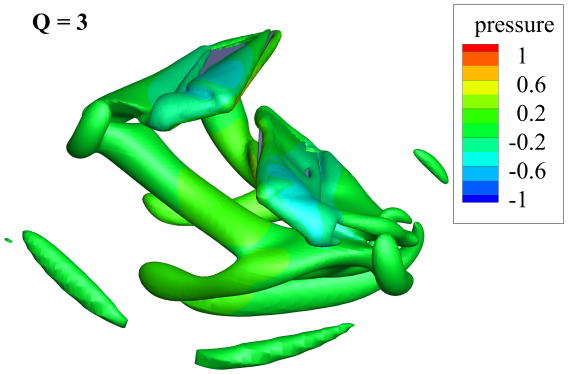

Figure 8: Vortical structures visualized by Q-criterion and colored by pressure at $tf = 5.73$.

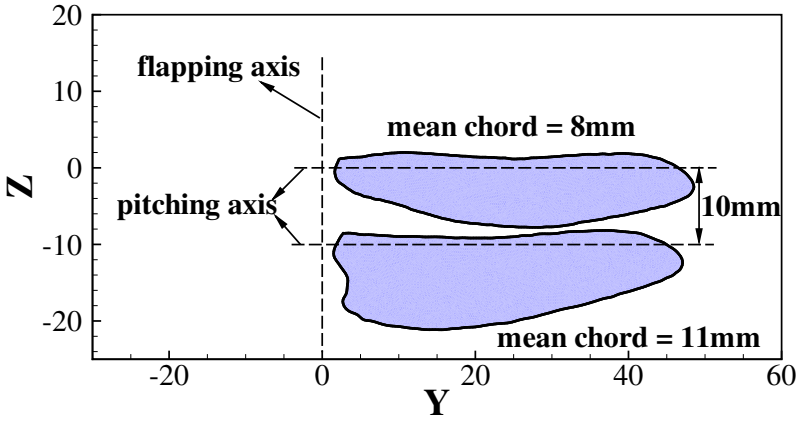

Figure 9: Geometric parameters of the tandem dragonfly wings.

from the pitching axis of each wing, which nominally matched that of real dragonflies. The flapping motions are prescribed as

$$Forewing: \quad \phi_f = \frac{\phi_0}{2}\cos(2\pi ft) \quad Hindwing: \quad \phi_h = \frac{\phi_0}{2}\cos(2\pi ft + \psi), \tag{21}$$

where ϕ_f and ϕ_h are the flapping angle for the forewing and hindwing, respectively. Here $\phi_0 = 80^o$ is the flapping amplitude and ψ is the phase angle between the flapping motion of the wings. The pitching motion is solved by equation 18 where the spring damping $C = 0$ and wing thickness $h = 0.01c$ for both wings.

The non-dimensional groups of the problem include the Reynolds number, mass ratio and the Cauchy number, which are respectively given by

$$Re = \frac{U_f L_f}{\nu}, \quad M_f = \frac{\rho_f h}{\rho c_f}, \quad M_h = \frac{\rho_h h}{\rho c_h}, \tag{22}$$

$$Ch_f = \frac{\rho\phi_0^2 f^2 c_f^3 L_f^2}{K_f}, \quad Ch_h = \frac{\rho\phi_0^2 f^2 c_h^3 L_h^2}{K_h}, \tag{23}$$

where U_f is the mean wingtip velocity at the leading edge of the forewing and $U_f = 2\phi_0 fL$. ρ_f and ρ_h are the wing density of the forewing and hindwing, respectively. K_f and K_h are the spring torsional stiffness of the forewing and hindwing, respectively.

The drag, lift and aerodynamic power coefficients and power economy for the forewing and hindwing are respectively defined as

$$C_{Df} = \frac{2F_{xf}}{\rho_f U_f^2 A_f}, \quad C_{Lf} = \frac{2F_{zf}}{\rho_f U_f^2 A_f}, \quad C_{Pf} = \frac{-\int_0^{c_f} \boldsymbol{f}_f \cdot \boldsymbol{V}_f dl}{0.5\rho_f U_f^3 A_f}, \quad PE_f = \frac{\bar{C}_{Lf}}{\bar{C}_{Pf}} \tag{24}$$

$$C_{Dh} = \frac{2F_{xh}}{\rho_h U_h^2 A_h}, \quad C_{Lh} = \frac{2F_{zh}}{\rho_h U_h^2 A_h}, \quad C_{Ph} = \frac{-\int_0^{c_h} \boldsymbol{f}_h \cdot \boldsymbol{V}_h dl}{0.5\rho_h U_h^3 A_h}, \quad PE_h = \frac{\bar{C}_{Lh}}{\bar{C}_{Ph}}, \tag{25}$$

where F_{xf}, F_{xh}, F_{zf} and F_{zh} are the hydrodynamic force acting on the forewing and hindwing in x and z direction, respectively. A_f and A_h are the surface area of the forewing and hindwing, respectively. $\boldsymbol{f}_f$ and $\boldsymbol{f}_h$ are the hydrodynamic traction on the forewing and hindwing,

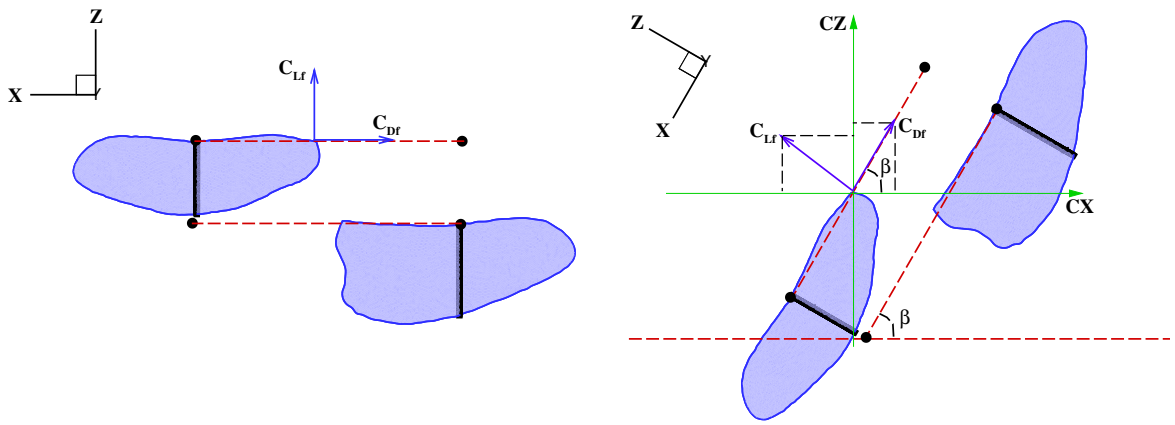

(a) horizontal stroke plane (b) rotated stroke plane

Figure 10: The schematic diagram of the rotating system.

respectively. $\boldsymbol{V}_f$ and $\boldsymbol{V}_h$ are the velocity of the forewing and hindwing, respectively. $\bar{C}_{Lf}$, $\bar{C}_{Lh}$, $\bar{C}_{Pf}$ and $\bar{C}_{Ph}$ are the cycle-averaged lift and aerodynamic power coefficient for the forewing and hindwing, respectively. U_h is the mean wingtip velocity at the leading edge of the hindwing. Then the total drag, lift and aerodynamic power coefficients and power economy of the two wings are

$$C_D = C_{Df} + C_{Dh}, \quad C_L = C_{Lf} + C_{Lh}, \quad C_P = C_{Pf} + C_{Ph}, \quad PE = PE_f + PE_h. \tag{26}$$

Figure 10 shows the schematic diagram of the rotating system. In the simulation, a horizontal stroke plane (figure 10(a)) is used. In the data processing stage, the whole system has been rotated into an inclined stroke plane angle $\beta = arctan(C_D/-C_L)$, to get a hovering state where the cycle-averaged drag force is zero. After rotating, the horizontal drag CX and vertical lift CZ coefficients are calculated as

$$CX_f = -C_{Lf}\sin\beta + C_{Df}\cos\beta, \quad CZ_f = C_{Lf}\cos\beta + C_{Df}\sin\beta, \tag{27}$$

$$CX_h = -C_{Lh}\sin\beta + C_{Dh}\cos\beta, \quad CZ_h = C_{Lh}\cos\beta + C_{Dh}\sin\beta, \tag{28}$$

$$CX = CX_f + CX_h, \quad CZ = CZ_f + CZ_h, \tag{29}$$

where CX_f, CX_h, CZ_f and CZ_h are the horizontal drag and vertical lift coefficients for the forewing and hindwing, respectively. CX and CZ are the total horizontal drag and vertical lift coefficients for the two wings.

A rectangular computational domain of size of $30c_f \times 30c_f \times 30c_f$ was used and the finest grid around the wing was $0.04c_f$, and the total grid number was 10.32×10^6. Six stroke cycles were simulated. Table 4 shows the domain size and grid data used in this study. Six stroke cycles are simulated and the last cycle is used to data analysis.

2.4.1 Effect of phase angle

Here the effect of phase angle is examined. Nine phase angle differences, $\psi = -180^o$, -135^o, -90^o, -45^o, 0^o, 45^o, 90^o, 135^o, 180^o, are considered. The Reynolds number $Re = 2000$, the Cauchy number $Ch_f = Ch_h = 0.15$ and mass ratio $M_f = M_h = 1$ were assumed. In order to get a stroke plane angle more closer to real dragonflies in hovering $[44^o, 60^o]$ (Norberg, 1975;

Table 4: Fluid domain size in $x-$, $y-$, and $z-$ directions, finest grid size, grid number, and CPU time t_w of one stroke cycle for the computation of the tandem dragonfly wing model. h: hour.

Sources	Domain size	Finest grid size	Grid number (10^6)	$t_w(h)$/ cycle
Present IB-LBM	$[30c_f, 30c_f, 30c_f]$	$0.04c_f$	10.32	0.71

Table 5: Cycle-averaged drag and lift coefficients for phase angle $\psi = 180^o$.

mean	forewing	hindwing	total
C_D	-0.369	-0.344	-0.713
C_L	0.3016	0.2361	0.5377
CX	0.0186	-0.0186	0
CZ	0.4763	0.4168	0.8931

Sun and Lan, 2004; Wang and Russell, 2007; Bode-Oke et al., 2018), a rest angle $\theta_0 = -40^o$ is chosen.

Table 5 shows the cycle-averaged drag and lift coefficients for phase angle $\psi = 180^o$. The stroke plane for phase angle $\psi = 180^o$ is $\beta = arctan(C_D/-C_L) = 52.98^o$. After rotating, the total horizontal drag CX is exactly zero.

Figure 11 shows the variation of the mean force coefficients with the phase angle. The variation of the absolute value of the drag force $|meanC_D|$ is much more evident than the mean C_L and CZ. The variation trend of the mean C_L and CZ is very similar.

Figure 12 shows the variation of power economy PE and stroke plane angle with the phase angle. The variation of PE is small as change of phase angle, while the stroke plane angle has a big variation at $\psi = -45$ and $\psi = 45$. But the all the stroke plane angle are still within the range $[44^o, 60^o]$ as reported in the literature (Norberg, 1975; Sun and Lan, 2004; Wang and

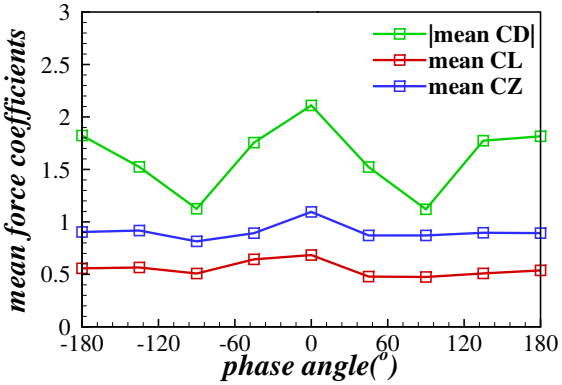

Figure 11: Phase angle vs mean force

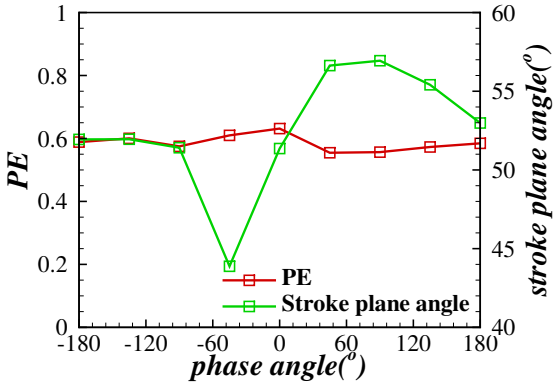

Figure 12: Phase angle vs power economy and stroke plane angle

Russell, 2007; Bode-Oke et al., 2018).

2.5 Conclusions

Validations of an IB-LBM solver for the computations of the hovering flight of prescribed kinematics for a rectangular flapping plate and a rigid fruit fly wing with passive pitching were performed. Good agreements of results between current computations and published data were observed, suggesting the present CFD solver can accurately compute the flow over flapping wing system. The high-fidelity and efficiency of the solver have also been highlighted through the grid convergence study and comparing the computational time with previously published data. The validated solver was then applied to simulate the passive pitching of tandem rectangular wings. This study provides additional data for benchmarking of CFD solvers in the simulation of passively pitching flapping wings. More detailed parameter investigations of passively pitching flapping wings under solitary and tandem configurations will be conducted in future studies.

3 Numerical study of passively pitching flapping wings in hovering flight

3.1 Introduction

Micro air vehicles (MAVs) are deemed the future of sensing capabilities, with great potential for use in environmental monitoring and homeland security (Shyy et al., 2010). The small form factor of an MAVs enables it access to previously inaccessible domains which can be useful for both military and civilian applications. However, the small size of MAVs requires that more efficient methods of controlling and flying them are employed. The design of MAVs face an inherent spatial constraint which scales inversely with the level of detectability and agility desired. The lack of space within an MAVs body to fit complex systems of actuators and motors to accurately manoeuvre the MAV is a recognised flaw. Flapping wing systems in insects have demonstrated the versatility and reliability of flapping wings to operate at small scales, and in numerous conditions. This has accelerated interest into the use of flapping wing systems in MAV designs (Platzer et al., 2008).

Insect flapping wing kinematics and aerodynamics have been studied extensively by researchers across the world. Insects make use of different methods for lift generation, including rapid pitch rotation (Dickinson et al., 1999), wake capture (Birch and Dickinson, 2003; Wang, 2005) and delayed stall (Birch et al., 2004; Ellington et al., 1996). Despite the availability of such knowledge in flapping wing lift generation performance, studies into the optimisation of flapping wings are still few and the implementation into MAV design still requires further study.

A key area of interest in the present study is the passive pitching phenomenon observed in insect flapping wing flight (Ishihara and Horie, 2016; Kolomenskiy et al., 2019; Lei and Li, 2020). Insect flapping wing flight involves wing pitch reversal where the insect periodically reverses its wing pitch to maintain a positive angle of attack throughout the wingbeat. Passive pitching is where the wing pitch reversal is done so without active actuation from the insect, enabled by the elastic, inertial and aerodynamic forces on the wing as it moves through the stroke (Ishihara and Horie, 2016; Kolomenskiy et al., 2019; Lei and Li, 2020). This phenomenon potentially reduces mechanical complexity and system mass required in a miniature robotic systems as it removes the need to actuate the wing in the pitch direction (Whitney and Wood, 2010). With the potential of passively pitching flapping wings to reduce the complexity of on-board actuator systems, the optimisation of passively pitching flapping wings for maximum flight performance is a key research interest.

The methods of optimisation of passively pitched flapping wing systems have varied across various studies with some opting to determine the best leading-edge wing trajectory (Lei and Li, 2020) and others investigated the variation of performance with wing shapes (Shahzad et al., 2016). Lei and Li (2020) also investigated the effects of the variation of torsional wing stiffness on passively pitching flapping wing performance. The present study uses computational fluid dynamics (CFD) to simulate the passive pitching flapping wing. A torsional spring model is used to model the passive pitching mechanism. This study is interested in the combination of torsional spring stiffness and wing shape to achieve the best performance in a passively pitching flapping wing. The main performance metric of interest is the power economy (PE), which indicates the extent of lift-generation of the wing in relation to the power required to operate it. PE will help quantify if a passively pitching flapping wing design can

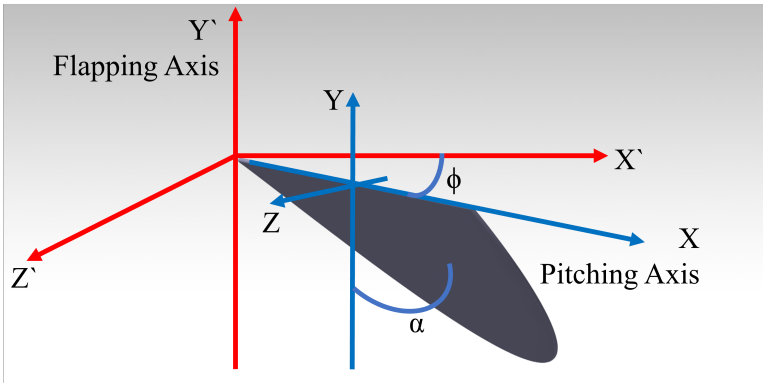

Figure 13: Definition of the pitching angle (α) and stroke angle (ϕ). The X-Y-Z coordinate system represents the body-fixed frame of reference while the X'-Y'-Z' coordinate system represents global coordinates.

be optimised for high lifts while maintaining low power requirements and simplicity of design.

Similar to previous efforts at optimising designs of artificial insect-like flyers, nature's design of insects provide a good starting point for optimisation (Platzer et al., 2008). In the current work, flapping wing models of different shapes and torsional spring stiffnesses were studied, with effort taken to mimic nature's designs and even beyond. The torsional spring stiffness was varied by changing the non-dimensional Cauchy number (Ch), which values were selected based on values known to produce realistic flapping wing kinematic. However, the extension beyond nature involved investigating the performance of wing shapes not characteristic of realistic insect wings. In addition, hovering was selected as the flight condition of interest as it is considered an important flight profile for potential MAV applications.

Section III describes the methodology used in creating the solver, including the kinematics, wing geometries, grid generation, as well as the numerical method. The verification of the numerical solver used is discussed in Secion IV and the validation case of a passively pitching fruit fly wing is shown in Section V. The simulation results and discussion are presented in Section VI. Finally, conclusions and further recommendations are shared in Section VII.

3.2 Methodology

3.2.1 Kinematics

The solver model was built based on two-angle flapping wing kinematics, where the two angles of concern are the pitching angle α and the stroke angle ϕ (Fig. 13). The deviation angle θ above the horizontal plane is taken as zero. In such a case, the leading-edge of the wing remains parallel to the horizontal plane throughout the flapping action. The stroke angle is prescribed to the flapping wing model at each time step and is defined by the sinusoidal function in Equation 30. The stroke amplitude ϕ_A, was set at the value of 140^o, which corresponds to the measured kinematics of fruit flies (Drosophila) (Altshuler et al., 2005). The flapping frequency f is a function of the wing tip velocity (U_{tip}), which was set as $0.1m/s$. The kinematics of the wing was applied to the solver via a user-defined function (UDF). This UDF defines all dynamic aspects of the model. The pitching angle α at each time step is a result of the torque on the wing from inertial and aerodynamic effects as it sweeps in the horizontal plane

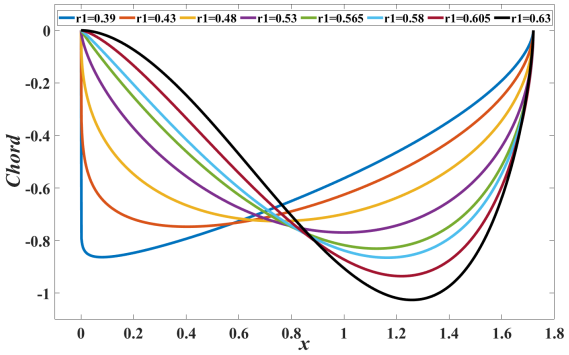

Figure 14: The increase of r_1 sees the area of the wing shift further outboard from the wing root, which is located at x = 0. Insects in nature are found to have wing shapes with r_1 within the range of 0.43 and 0.563 (Shahzad et al., 2016).

through the fluid. At each time step, the angular acceleration due to the torque on the wing is calculated and further integrated to get angular velocity $\dot{\alpha}$. The pitching axis is located at the leading edge of the wing and the flapping axis is located at the hinge as seen in Fig. 13. A realistic pitching kinematic sees the pitching angle remain relatively constant through the mid-stroke and changes rapidly at the wing stroke reversals at the end of each stroke. This rapid change of pitching angle during the stroke reversal of the stroke is characteristic of insect flapping wing flight (Dickinson et al., 1999).

$$\phi = -\phi_A \sin(2\pi f t), \quad U_{tip} = 2 f \phi_A R, \quad \alpha_1 = \alpha_0 + \dot{\alpha}\Delta t, \tag{30}$$

$$Ch = \frac{\rho \phi_A^2 f^2 c^3 R^2}{K_s}. \tag{31}$$

In this model, the passive pitching mechanism was modelled with a torsional spring at the wing hinge, which provides the elastic torque to the wing. The torsional spring stiffness is further defined by the non-dimensional Cauchy number (Ch). Ch represents the ratio of the aerodynamic forces acting on the wing and the elastic torsional spring force at the wing hinge. This ratio is used to vary the stiffness of the torsional spring while maintaining a realistic flapping wing kinematic. The values of Ch were selected based on values found in literature; these values have been shown to create realistic passive pitching flapping wing kinematic (Lei and Li, 2020; Ishihara et al., 2009b).

3.2.2 Wing geometry and mesh generation

Eight different wing shapes were studied and each were generated based on the radius of first moment of area $\bar{r}_1$, which defines the chord length of different points along the spanwise direction. The wing shapes were modelled with a constant planform area of 1.0 m^2 and the aspect ratio AR was maintained at 2.96 for all cases. Key parameters used in the present work were defined with non-dimensional numbers. As such, this high-fidelity model can be scaled and controlled based on characteristic non-dimensional numbers such as Re, Ch or AR, for targeted studies. As r_1 increases, the planform area of the wing shifts further outboard from

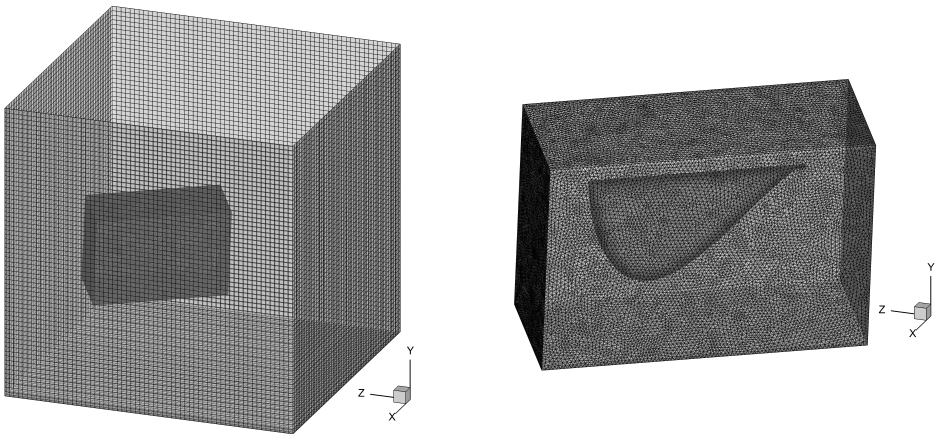

(a) A domain size of 10c x 10c x 10c was sufficient

(b) The fine overset region captures key flow structures

Figure 15: The mesh used for both the background and the overset region closer to the wing added up to about 3.5×10^6 cells. These were found to be sufficient to obtain accurate results for the numerical study.

the wing root. The equations for wing shape generation were adopted from Ellington (1984):

$$\bar{r}_1 = \int_0^1 \bar{c} \cdot \bar{r} d\bar{r}, \quad \overline{r_2} = 0.929 \left(\bar{r}_1\right)^{0.732}, \tag{32}$$

$$p = \bar{r}_1 \left(\frac{\bar{r}_1 \left(1 - \bar{r}_1\right)}{\overline{r_2}^2 - \bar{r}_1^2} - 1 \right), \quad q = \left(1 - \bar{r}_1\right) \left(\frac{\bar{r}_1 \left(1 - \bar{r}_1\right)}{\overline{r_2}^2 - \bar{r}_1^2} - 1 \right), \tag{33}$$

$$\beta(p,q) = \int_0^1 \bar{r}^{p-1}(1-\bar{r})^{q-1} d\bar{r}, \quad \bar{c} = \frac{\bar{r}^{p-1}(1-\bar{r})^{q-1}}{\beta(p,q)}, \tag{34}$$

where $\bar{c}$ and $\bar{r}$ are the normalised chord length and distance from the wing root in the spanwise direction. $\bar{c}$ and $\bar{r}$ are normalised by the mean chord c and wingspan, R respectively, as determined from the AR. $\bar{r_1}$ and $\bar{r_2}$ are the non-dimensional radii of the first and second moments of area of the wing, respectively. Finally, the beta function $\beta(p,q)$ is defined by $\bar{r_1}$ and the resultant variables p and q. The values of $\bar{r_1}$ chosen for wing shape generation were chosen between 0.39 and 0.63. Although the $\bar{r_1}$ of most insect wings fall within the range of 0.43 and 0.563 (Ellington, 1984), the present work explores if there are wing shapes that are more optimal than those inspired by nature.

An overset mesh as shown in Fig. 15 was used in this study, where the region close to the wing is a separate finer region to the coarser background mesh. A uniform cubic mesh was used for the background mesh while a triangular mesh is used in the finer region. Inflation layers were also used at the surfaces of the wing to accurately capture the boundary layers on the wing. Further modifications were made to the mesh to capture the curvatures of the wing tips. The mesh near the curved wing tips were essential for calculation of the wing edge vortices which will be essential to understand the aerodynamics of the flapping wing flight. The fine region had approximately 2.5×10^6 cells while the background mesh had about 1.0×10^6 cells. The use of the overset mesh enabled highly accurate and detailed flow field calculations around the wing, at a reasonable computational cost. The verification of the reliability of these mesh settings are explained further in Section IV.

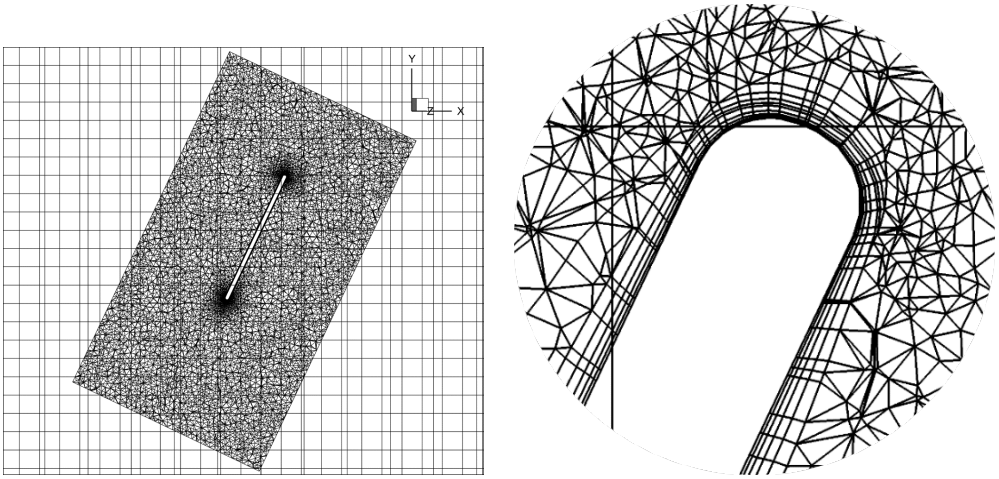

(a) Cross section of overset mesh region, showing the mesh refinements around the wing

(b) Inflation layers used on the wing surface enabled boundary layers to be captured accurately

Figure 16: Additional mesh treatments were made close to the wing surface to best capture the flow structures around the wing.

3.2.3 Governing equations and numerical method

The governing equations solved in the numerical solver are the continuity equation and the conservation of momentum equation, which together make up the incompressible Navier Stokes equation:

$$\frac{\partial u_i}{\partial x_i} = 0; \quad \frac{\partial u_i}{\partial t} + \frac{\partial u_i u_j}{\partial x_j} = -\frac{\partial p}{\partial x_i} + \frac{1}{Re}\frac{\partial^2 u_i}{\partial x_i \partial x_j}, \tag{35}$$

where $u_{i,j}$ are the velocity components, p is the pressure, and Re is the Reynolds number.

A finite volume method (FVM) was used to solve the above equations. A pressure-based solver algorithm was employed, in which the continuity constraint of the velocity field is achieved through solving a pressure equation. This pressure equation is derived from the continuity and momentum equations, where a pressure correction is applied to the velocity field.

A laminar flow model was used in the numerical solution as the Reynolds number (Re) was kept constant at 300. Relative densities of the wing and the fluid was set by the mass ratio (M). The value of M dictates the relative effects of the aerodynamic forces versus the inertial forces and is generally kept at 1.0 for rigid wings (Luo et al., 2010). For the purpose of this study, this mass ratio covers a wide range of species of insects such as fruit flies and honeybees (Lei and Li, 2020). The equations used to calculate the key parameters used are:

$$\mathrm{Re} = \frac{\rho U_{tip} R}{\mu}, \quad M = \frac{\rho_s h}{\rho c}, \quad h = 0.03c, \tag{36}$$

where R is the wingspan, f is the flapping frequency, h is the wing thickness, and c is the mean chord length of the wing.

The passive pitching of the flapping wing is enabled by the aerodynamic and inertial forces that act on the wing as it sweeps through the fluid domain. The elastic torque on the wing from the torsional spring at the wing hinge also contributes to the passive pitching on the wing

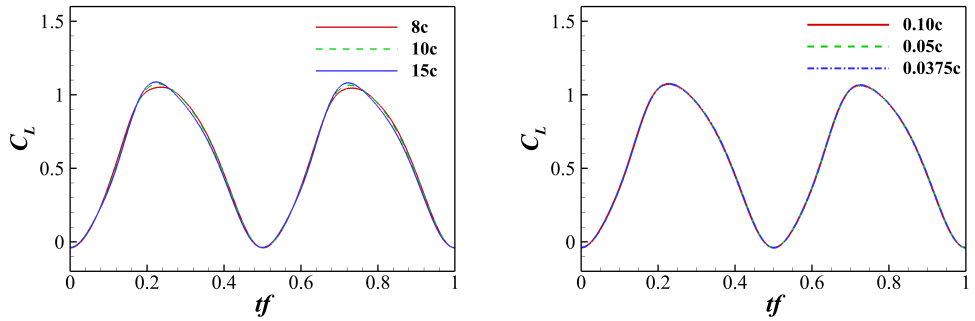

(a) Comparison of C_L with different domain sizes

(b) Comparison of C_L with different overset grid sizes

Figure 17: Comparison of the C_L from the domain independence study and grid independence study. Both revealed that a domain size of 10c and a overset region grid size of 0.05c were sufficient for a good balance of solution accuracy and computational expense.

by providing the restoring torque when the wing is pitched away from its neutral (vertical) position. These are shown in Eq. 37. I_{xx} and Ixy are components of moment of inertia of the wing. At each time step, the position and rotation of the wing is updated according to the velocities of the wing calculated in the preceding time step. The aerodynamic moment M_{aero} was also calculated at each time step based on the surface pressure on the wing, integrated over the wing surface. These calculations were done within the applied UDF.

$$I_{xx}\ddot{\alpha} = M_{aero} + (-K_s\alpha) + I_{xy}\ddot{\phi}\cos\alpha + \frac{1}{2}I_{xx}\dot{\phi}^2\sin 2\alpha. \tag{37}$$

3.3 Solver verification

Multiple independence studies were conducted to verify that the discretisation used in the solver model were sufficient. In terms of the control volume discretisation, both a domain independence and a grid independence study were done and were shown in Fig. 17. The domain independence study in Fig. 17(a) confirmed that a domain size of $10c$ is sufficiently large that the solution is independent of the domain boundaries. From the grid independence study as shown in Fig. 17(b), it is found that there is minimal difference in results from the grid sizes defined. The final choice of 0.05c was made based on the requirements of getting detailed flow visualisation and at reasonable computational expense.

A time step independence study was also conducted to verify that the time domain discretisation of the solver model was sufficiently fine for solution accuracy. Figure 18 shows that a time step size of 0.2s was discrete enough for reliable solver calculations. This time step size also allowed the collection of key flow structure visualisation data.

3.3.1 Solver validation

Validation of the solver was conducted with a wing shape of $\bar{r}_1$=0.48, which resembles that of a fruit fly's wing. Results from this case were compared with the results from Lei and Li (2020) and Huang et al. (2021) where passively pitching fruit fly wings were also studied numerically. Lei and Li (2020) used an immersed boundary-Navier-Stokes equation solver while Huang et al. (2021) used an immersed boundary-lattice Boltzmann method solver. The non-dimensional

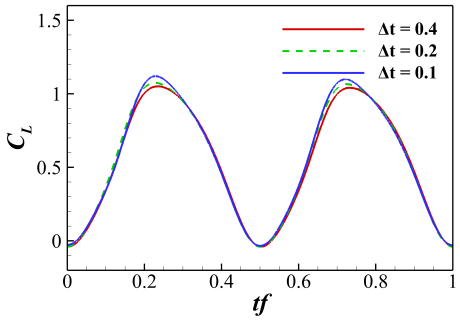

Figure 18: A time step size of Δt=0.2s was sufficient for good solution accuracy.

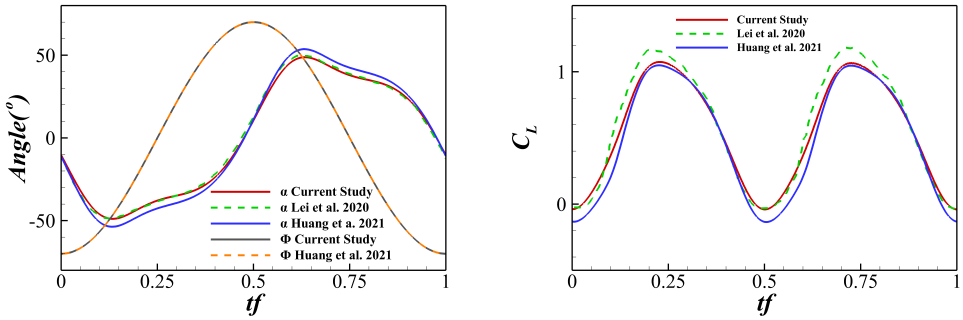

(a) Comparison of time history of angles (b) Comparison of time history of C_L

Figure 19: Comparison of the pitching angles, stroke angles and lift coefficients obtained between Lei and Li (2020), Huang et al. (2021) and this study. The results show a close agreement of the results and provides confidence for the solver used in this study.

parameters used were consistent in all three cases, which were Re=300, Ch=0.15 and M=1.0. Figure 19 shows that the pitching angle and the time history of the lift coefficient from this study agree well with the results from the two referenced studies. The agreement of the results from three different solver set ups provided confidence in the reliability of the present work's solver.

3.4 Results and discussion

The investigation of passively pitching flapping wing performance was conducted by changing r_1 and Ch, which were key variables relating to the inertial and elastic torque on the wing, respectively. The results reveal that there is indeed an optimal combination of r_1 and Ch that achieves an optimal flapping wing flight performance at Re=300. The trends observed in flapping wing performance relating to the changes in Ch and r_1 are discussed in this section. The drag coefficient C_D, lift coefficient C_L, power coefficient C_P, and power economy (PE) are defined as:

$$C_D = \frac{2F_D}{\rho {U_{tip}}^2 S}, \quad C_L = \frac{2F_L}{\rho {U_{tip}}^2 S}, \quad C_P = \frac{2P}{\rho {U_{tip}}^3 S}, \quad PE = \frac{\bar{C}_L}{\bar{C}_P}, \tag{38}$$

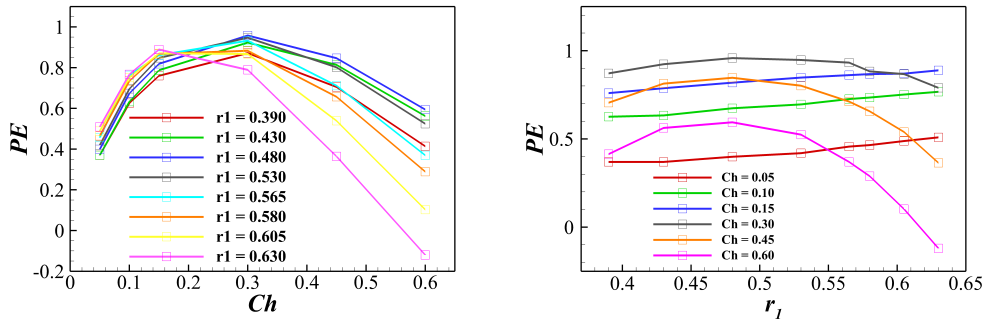

(a) Power economy peaks where Ch is about 0.30 and diverges across the wing shapes as Ch increases

(b) Power economy varies differently with wing r_1 as Ch increases past 0.30

Figure 20: PE follows the same trend across all wing shapes as Ch changes, with most curves peaking at Ch=0.30. Ch=0.30 represents a notable transition point for trends observed in PE. Across the different r_1, the difference in performance is obvious at higher Ch.

where F_D and F_L are the drag and lift force, respectively. P is the power required by the wing and S is the planform area of the wing. $\bar{C}_L$ and $\bar{C}_P$ are the mean lift coefficient and mean power coefficient, respectively. At each time step, P was calculated by taking the sum of the pitching power and stroke power, each of which were calculated by taking the product of the torque around the axis of rotation and the angular velocity about that axis. The main performance criteria in this discussion is PE, given its significance for optimising artificial design at minimal cost basis for lift.

3.4.1 Power economy

PE accounts for the costs associated with producing lift in the form of the power required to produce that lift. This cost could be significant for insects since the power inputs can be severely constrained by the small form factor. The variation of PE with Ch in Fig. 20(a) shows that for most of the wing shapes, peak PE is found at Ch=0.30 and for Ch greater than 0.30, the mean lift coefficients for all wing shapes decreases, with some decreasing more sharply. Furthermore, Fig. 20(b) shows that with r_1, there are two different sets of observations to be made, one for Ch less than 0.30 and another for Ch greater than 0.30. For the former, PE increases slightly as r_1 increases while the latter shows a local peak established at r_1=0.48 before PE drops. The trends observed in PE showed a notable dependence of PE on Ch, with a clear transition point being Ch=0.30. Thus, further investigation was carried out on the components of PE, C_L and C_D (analogous to C_P, and their variation with Ch, to better understand the variation of PE with Ch.

The variation of PE with r_1 was also of interest as the observed trends showed that the difference in performance across the wing shapes is more pronounced at the higher Ch. This exaggerated difference in performance across the wing shapes at the higher Ch was also further investigated by analysing the variation of C_L and C_D with r_1.

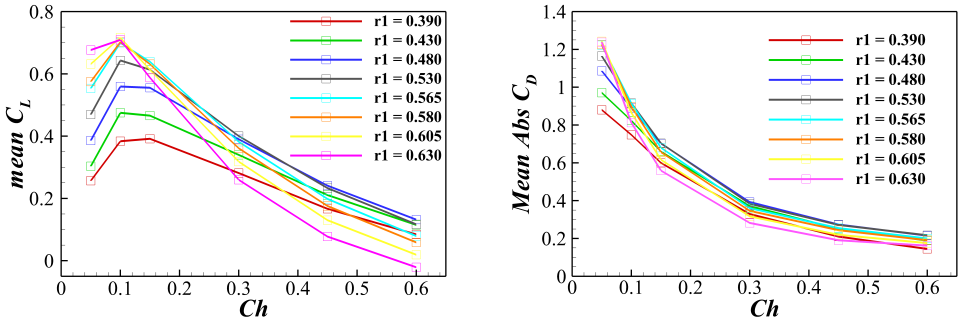

(a) $\bar{C}_L$ vs. Ch (b) $|\bar{C}_D|$ vs. Ch

Figure 21: The lift and drag variation with Ch reveal that the decrease in PE at higher Ch is due to the drop in lift-generation more than an increase in power required. For lift-generation, wings with high r_1 perform very well at low Ch but also perform the worst at high Ch. $|\bar{C}_D|$ for all wing shapes decreases as Ch increases.

3.5 Cauchy number dependence

Figure 21(a) shows that as the Ch increases, the wing shapes with r_1=0.580, 0.605 and 0.630 see a steeper decrease in $\bar{C}_L$. As Ch increases past 0.30, $\bar{C}_L$ of these three wing shapes are also amongst the lowest in the set. In terms of purely lift-generation, a wing shape with high r_1 will perform slightly better at low Ch while also suffer disproportionately more at high Ch. The mean absolute drag coefficient ($|\bar{C}_D|$) was studied as it is analogous to the power required and is intuitive to analyse in aerodynamic analysis. Figure 21(b) illustrates that as Ch increases, the mean absolute drag coefficient curves for the different wing shapes follow largely the same rate of decrease and converge to the same value. The higher Ch represents the softer springs, and thus the wings behaved increasingly like a flat plate laid parallel to an incoming flow. This shows that the decrease in PE as Ch increases, is largely due to the decline in lift-generating performance at higher Ch. Thus, the variation of lift-performance with Ch was further investigated in the next subsection. The time profiles of the pitching angle and the lift coefficient were investigated for a wing with r_1=0.605, at the different values of Ch. Ch relates directly to the torsional spring stiffness of the wing hinge, with a larger value of Ch representing a softer spring. Figure 22(a) shows that in general, as the spring stiffness decreases, the pitching amplitudes for the wing increases as expected. However, as shown in figure 22(b), the trend in lift-curves do not follow the same sequential trend across all values of Ch. Some consistent observations are that as Ch increases, the peak pitch of the wing is delayed further into the flapping cycle. This trend is also seen in the time history of C_L. Additionally, for values of Ch equal to or greater than 0.30, negative lift is generated shortly after starting the stroke, after wing pitch reversal. Based on Fig. 22(b), the phases in the flapping cycle which sees the greatest difference in lift-performance across the different values of Ch are at tf=0.20 and tf=0.70. Thus, the flow fields at tf=0.70, for the case of r_1 = 0.605 at various Ch are shown in Fig. 23. The wake structure were visualised by calculating the iso-surfaces of Q-criterion and these iso-surfaces were coloured by pressure. At the lower Ch, the vortices around the wing are much larger in size and are stronger based on the suction pressure they create. This indicates that the lift and drag on the wing are also greater in magnitude. For the lower Ch, the low pressure region on the upper surface of the

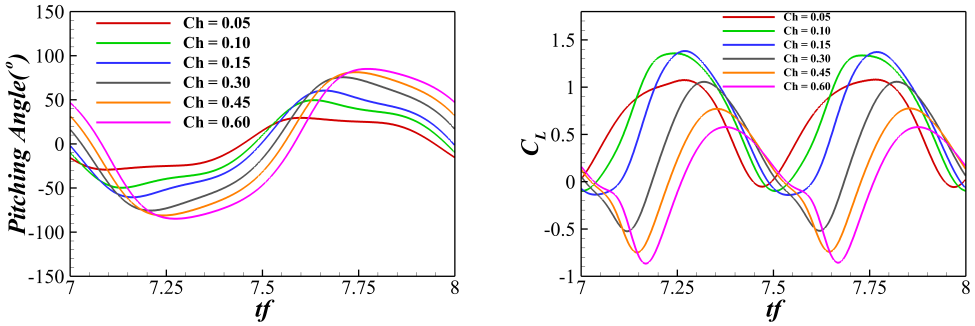

(a) Time history of the pitching angle (α)

(b) Time history of C_L

Figure 22: Comparison of the pitching angles, and lift coefficients obtained between cases of $r_1 = 0.605$ at different values of Ch. While trends in pitch angle are sequential, the variation in lift-generation is not; the lift curves change in shape and show negative lift for values of Ch greater than or equal to 0.30.

wing indicates positive lift-generation.

The leading edge vortex (LEV), trailing edge vortex (TEV) and tip vortex (TV) are clearly visible in Fig. 23(e), which is at a low Ch of 0.05. For the higher Ch, as seen in Fig. 23(g) and Fig. 23(h), the vortex structures are much smaller and less obvious. Correspondingly, the upper surfaces of the wings with higher Ch is at a higher pressure than the bottom surfaces, creating a suction downwards on the wing. This negative lift generation caused at the wing pitch reversals is not observed at Ch less than 0.30. The wings with higher Ch pitch to a larger α, resulting in wake capture lift-generation being less effective as the wing does not intercept as much of the wake from the previous stroke. At the same time, the LEVs, which are responsible for majority of the lift in flapping wing flight, weaker for the high Ch. These effects fully manifest for Ch equal to or greater than 0.30, resulting in the sharp decline in lift past Ch=0.30, for the same wing shape.

3.6 Wing shape dependence

The trends observed of $\bar{C}_L$ and $|\bar{C}_D|$ in Fig. 24 across r_1 reveals that for all Ch, aerodynamic performance follow a similar pattern. The peaks of $\bar{C}_L$ and $|\bar{C}_D|$ shifts towards the higher r_1 as Ch decreases. These peaks are useful to narrow down a choice of wing shape for a given Ch, since it is optimal to maximise lift while minimising drag. For instance, we observe that for Ch=0.10, while peak $\bar{C}_L$ occurs at r_1=0.605, maximum $|\bar{C}_D|$ occurs at r_1=0.530. Furthermore, the comparison of the PE across the different r_1 at a Ch of 0.60 showed that the differences were large across the wing shapes. $|\bar{C}_D|$ remained relatively constant at Ch=0.60, which was expected from the soft torsional spring. Hence, it is noted that the vastly different performance at high Ch is more dependent on lift than drag.

The time profiles of lift were analysed across the different r_1, along with the flow structure visualisation to supplement the discussion. Figure 25 shows that at Ch=0.60, most wing shapes showed a similar time profiles of lift. Generally, the wing shapes experienced maximum lift at tf=0.35 and tf=0.85 while minimum lift occurred at tf=0.15 and tf=0.65. Exceptions were observed for the the wings with r_1=0.390 and r_1=0.630 at tf=0.15 and tf=0.65, where the two wings had a delayed negative lift response while the other wing shapes saw peak

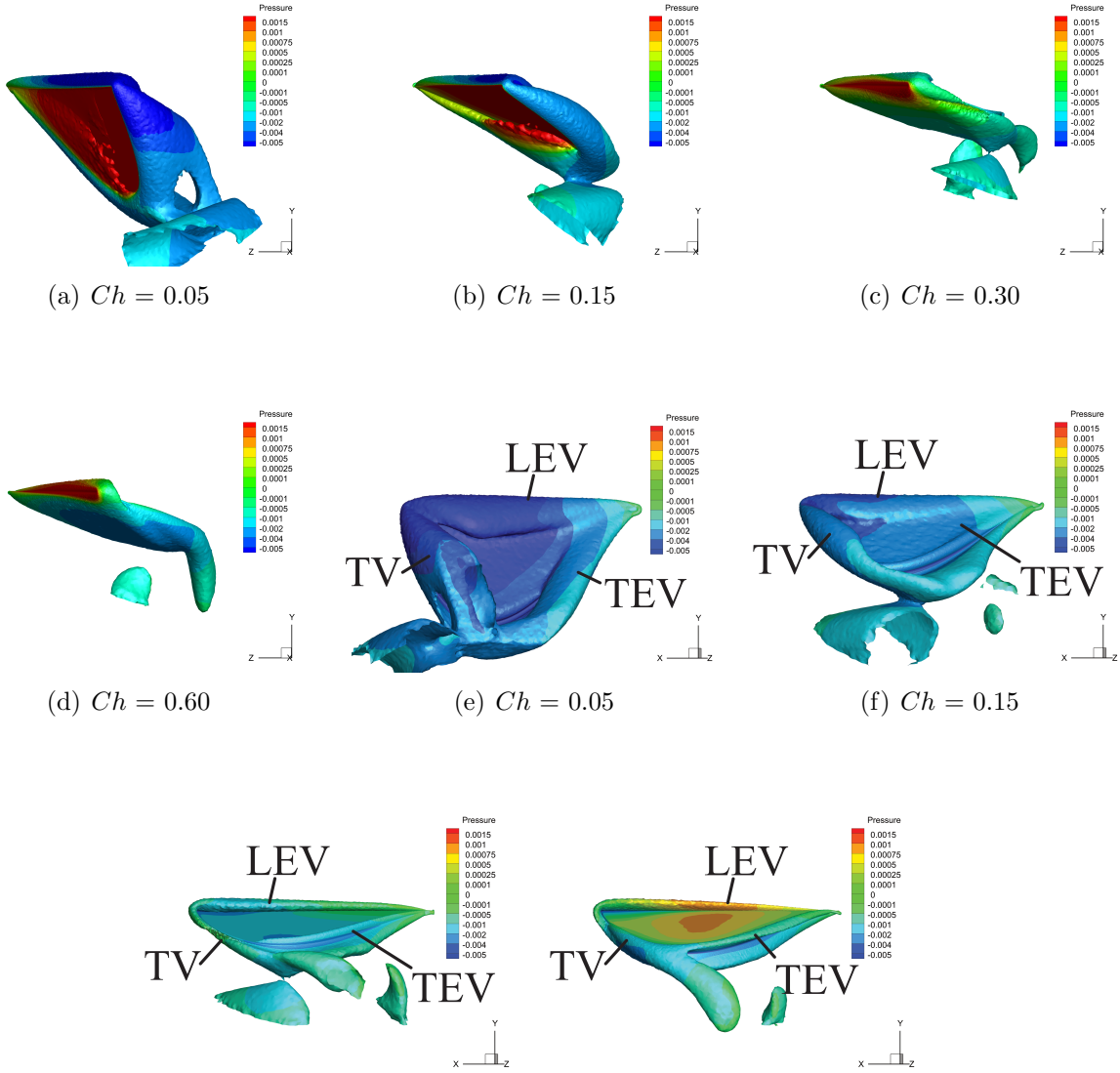

(a) $Ch = 0.05$ (b) $Ch = 0.15$ (c) $Ch = 0.30$

(d) $Ch = 0.60$ (e) $Ch = 0.05$ (f) $Ch = 0.15$

(g) $Ch = 0.30$ (h) $Ch = 0.60$

Figure 23: Instantaneous flow structure comparison across different Ch for a wing with r_1=0.605 at $tf = 0.70$. Two views are shown for the wing with different values of Ch. For the lower Ch, pressure suction caused by the vortices are stronger, resulting in larger lift and drag compared to the wings with higher Ch.

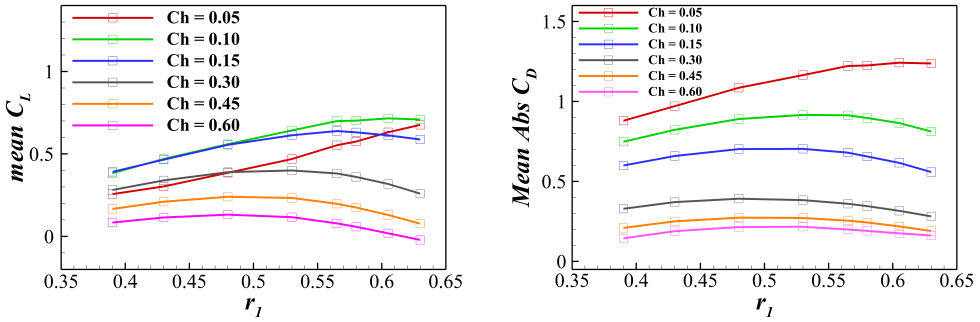

(a) $\bar{C}_L$ vs. r_1 (b) $|\bar{C}_D|$ vs. r_1

Figure 24: The variation of $\bar{C}_L$ and $|\bar{C}_D|$ with wing shape. At the higher Ch, $|\bar{C}_D|$ remains relatively constant.

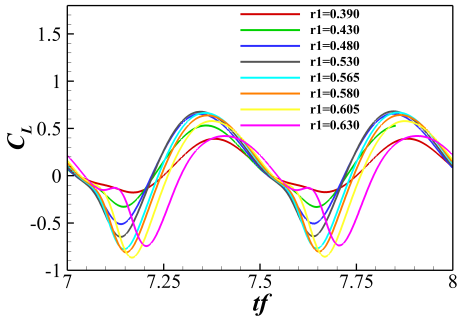

Figure 25: The time profile of lift across the different wing shapes.

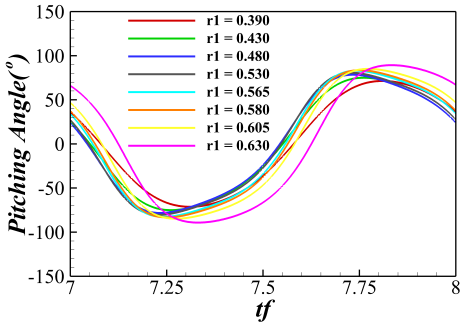

Figure 26: The time profile of pitching angle across the different wing shapes.

negative lift. With Ch=0.60, r_1=0.390 produced one of the highest $\bar{C}_L$ while r_1=0.630 was the worst performer.

The wing kinematics for all wing shapes were also analysed over a flapping cycle. Figure 26 shows that there is a delayed pitching behaviour observed as r_1 increases and this delay gets increasingly larger as r_1 increases. Interestingly, the delayed pitching behaviour is also seen for a wing shape with r_1=0.390. Both these wing shapes have a larger maximum chord length which provides a larger moment arm in the pitching direction. The delayed pitch seems to have a large influence on the lift-generating performance of the wing, as r_1=0.390 and 0.630 are correspondingly the best and worst performers in lift.

Visualisation of the flow structure around the wing revealed some key differences across the wing shapes. The snapshot was taken at tf=0.65, as there was a significant difference in lift across all the wing shapes, as seen in Fig. 25. At tf=0.65, all wings experienced little or negative lift, to varying degrees. This is seen as a lower pressure region on the bottom face of the wings in Fig. 27. The wake structure of the wings with r_1=0.390 and 0.630 show larger and stronger LEVs, TEVs and TVs, which corresponds to the less negative lift observed at tf = 0.65. Both these wing shapes have relatively longer maximum chord lengths and the high pressure region is observed only on a part of the upper wing surface near the trailing edge tip. This creates an instantaneous torque which helps maintain the wing at a high angle of attack for that phase of the flapping cycle and causes the delayed pitching. The vortices around the wings with r_1=0.480 and 0.565 are relatively weaker, and a high pressure region is seen across the top surfaces, causing a stronger downward suction on the wing and more negative lift. Additional root vortices (RV) were also observed for the wing shapes with lower r_1.

3.6.1 Optimal performance configuration

The variation of PE with both Ch and r_1 is shown in Fig. 20. It is observed that the optimal Ch-r_1 pair for a passively pitching flapping wing at Re=300 lies in the middle where Ch=0.30 and r_1 is between 0.48 to 0.53. These trends provide insight into the relationship between wings shape and hinge stiffness to maximise performance. It is noted that in the optimal region, there is a range of wing shapes that are relatively similar in performance. Fig. 28(b) shows the optimum combination of Ch and r_1 to achieve the maximum lift.

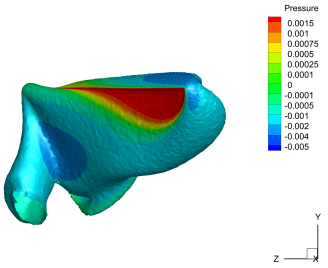

(a) $r_1 = 0.390$

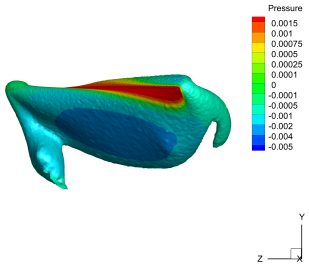

(b) $r_1 = 0.480$

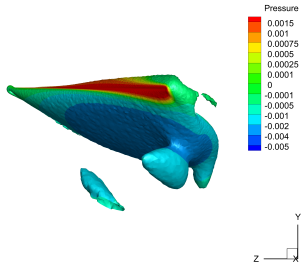

(c) $r_1 = 0.565$

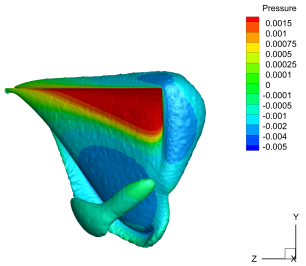

(d) $r_1 = 0.630$

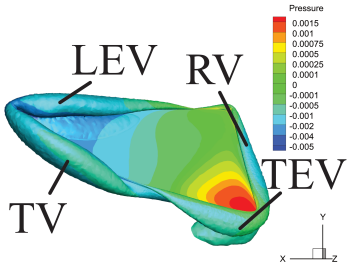

(e) $r_1 = 0.390$

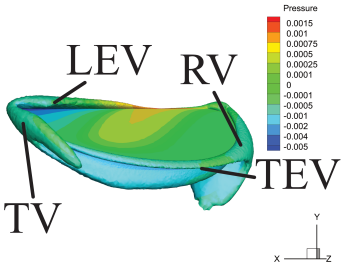

(f) $r_1 = 0.480$

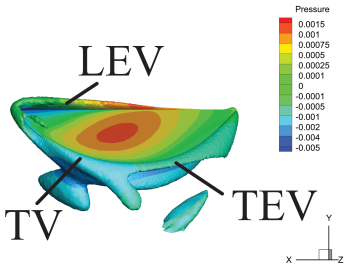

(g) $r_1 = 0.565$

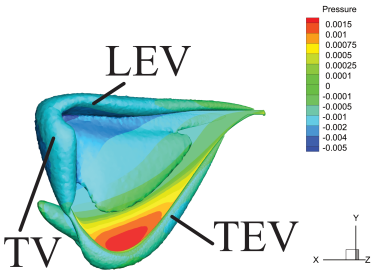

(h) $r_1 = 0.630$

Figure 27: Instantaneous flow structure comparison across different r_1 for a wing with Ch=0.60, at $tf = 0.65$.

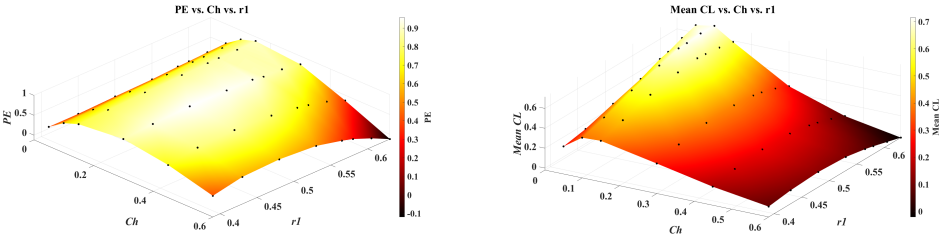

(a) PE vs. Ch vs. r_1 (b) $\bar{C}_L$ vs. Ch vs. r_1

Figure 28: The optimal configurations for PE lies within the range of r_1=0.48 to r_1=0.53 and Ch=0.30. For maximum lift, the optimal combination of Ch and r_1 is around 0.10 and 0.60 respectively.

3.7 Conclusion and further recommendations

A FVM model for the simulation of passively pitching flapping wings, at different wing shapes and torsional spring stiffness has been successfully built. Verification and validation of the current solver for computing passively pitching flapping wing flight in hover were completed. The results agree well with the validation cases referenced and confirms the high fidelity of the solver used. In this study, the results reveal that there exists an optimum combination of wing shape and torsional spring stiffness for the best PE. PE was chosen as the key performance metric since the costs associated with generating lift is significant for miniature flyers such as insects which has severe spatial constraints. The best configuration for maximum PE (at Re=300) is with r_1=0.48 and Ch=0.30.

The current work also included a study into the aerodynamics of the passively pitching flapping wings simulated and that revealed some key observations. The further study revealed that lift-generation for Ch greater than or equals to 0.30 suffers due to weak wake structure and lack of wake capture. Furthermore, drag remains relatively similar for higher Ch, indicating that PE is more lift-dependent at higher Ch. The effect of changing r_1 was also investigated and revealed that at the extremes of low r_1 and high r_1, delayed pitching occurs. This delayed pitching allows better lift-performance for the low r_1 but causes lift-performance to suffer at higher r_1.

The wealth of data collected for the 48 different combinations of r_1 and Ch can be further studied to provide a more comprehensive understanding of how passively pitching flapping wing performance varies with wing shape and torsional spring stiffness. Furthermore, the high fidelity model can easily be used for further research into other areas of passively pitching flapping wing flight. These other interest areas may include the Re-sensitivity or natural frequency of passive pitching flapping wing flight. As the present work made use of non-dimensional numbers as key parameters, the current model can also be scaled accordingly to meet the needs of other research areas on passively pitching flapping wing flight. Finally, this numerical model can also be paired with experimental methods to further improve our understanding of compliant musculoskeletal dynamics of wind actuation in insects and artificial platforms.

4 Performance of passively pitching flapping wings in the presence of vertical inflows

4.1 Introduction

Wing pitching motion in insects has been hypothesized to be predominantly a passive phenomenon induced by inertial and aerodynamic effects with some active input at the wing hinge (Bergou et al., 2010, 2007; Ishihara et al., 2009b; Beatus and Cohen, 2015; Ennos, 1988b). Morphological studies on dipteran wings have reported the existence of high torsional flexibility around the basal region of the wing which directly influences the torsional dynamics around the span-wise direction (Ennos, 1987, 1988a; Ishihara, 2018). Achieving desired kinematics with the minimum weight and complexity of wings, muscles and other actuating structures, and neurological control mechanisms provides an evolutionary imperative towards maximum use of passive elements in wing motion and deformation (Liu et al., 2016). Inspired by insect flight, passively pitching flapping wings have been implemented in micro aerial vehicle (MAV) designs due to the relatively simple actuation system governing only the flapping component of the kinematics (Wood et al., 2013; James et al., 2018; Farrell Helbling and Wood, 2018). The pitching angle of this kind of flapping wing can be passively modulated by an elastic hinge acting as a torsional spring which balances the moments resulting from fluid mechanic and inertial forces (Bergou et al., 2007; Moore, 2015; Lee et al., 2013).

Interaction between a passive pitching flapping wing and its surrounding fluid is quantified by a non-dimensional parameter, Cauchy number Ch, which is the ratio of fluid mechanic forces to elastic reaction forces (Ishihara et al., 2009b,a; Whitney and Wood, 2010). Assuming all flapping parameters and wing geometry as constant, the pitch angle of a wing with a low Cauchy number remains relatively constant during flapping motion, leading to high drag and input power (thus low efficiency) because the elastic moment offsets the effect of the aerodynamic moment. In contrast a wing with a high Cauchy number tends to orient parallel to the relative flow direction during the flapping stroke resulting from dominant effects of the fluid mechanic moment (Sum Wu et al., 2019; Kolomenskiy et al., 2019; Lei and Li, 2020). Tuning the Cauchy number in the construction of passive-pitching flapping wings results in a balance between minimising input power while maintaining the required mean lift, or equivalently increasing the lift for a given input power. Numerical simulations of 3D wing performed by Hao et al. (2019) revealed that with appropriate Cauchy number the mean lift produced by a passive-pitching flapping wing can be enhanced by 10% compared to a flapping wing performing prescribed pitching at the same aerodynamic efficiency.

An important requirement in preparation of MAVs with passive-pitching flapping wings for outdoor operations is the capability to overcome the effects of wind disturbances, likely to be encountered during flight in cluttered environments. This raises important questions of how the time-history of the wing pitching motion, and consequently unsteady aerodynamic effects are altered by freestream disturbances compared to quiescent hovering, as well as how the Cauchy number should be adjusted in response to inflow perturbations. Most studies on passive-pitching flapping wings have been in quiescent flow, that is unrepresentative of natural conditions, and our understanding of impacts of freestream disturbances on their performance is limited. One study examined the aerodynamic performance of a passively pitching flapping wing through uniform frontal flow, which noted that the mean lift can be enhanced up to 40% as the gust ratio, the ratio of frontal flow speed to the maximum wing velocity, increased from

0 to 1 (Li et al., 2018).

In the present study, we experimentally explored the interaction between passive-pitching flapping wings and inflow perturbations oriented upward or downward with respect to the stroke plane. Such perturbations are ubiquitous in outdoor environments such as in proximity to buildings, under tree canopies, or in mountainous terrain with updrafts and downdrafts (Mohamed et al., 2012). As the Ch has a determining influence on the performance of flapping wings under quiescent conditions, to test its significance under the effects of vertical perturbations, we introduced a range of steady vertical flows with constant velocity over a flapping wing where the Ch was varied to span three orders of magnitude. Force measurements were taken through a 6-axis force/torque (F/T) sensor to gain an understanding of the effect of the vertical inflow on the mean aerodynamic performance and transient aerodynamic characteristic of the wing. The pitching angle of the wing was captured by a camera to relate lift and drag coefficients and kinematic features for a range of upwards and downwards vertical inflows at different Cauchy numbers.

4.2 Experimental set-up and procedure

4.2.1 Flapping wing rig

The experiment consisted of a dynamically scaled, single flapping wing operated in a $900mm \times 900mm \times 600mm$ water tank (Figure 29 (a)). The wing was rectangular with chord $51mm$ and span $150mm$ (Table 6), giving over six chord length separation between the wingtip and the tank walls at all times and reducing wall effects. The flapping rig itself consisted of a servo motor (RoboStar SBRS-5314HTG 280°, Digital Gear High Voltage Robot Servo) controlling the flapping motion of the wing via the main shaft as shown in Figure 29 (a). A six-axis force/torque sensor (ATI Nano 17-IP68) was mounted between the main shaft of the flapper and the root of the wing. The flapping rig was attached to a vertical linear actuator (Multi-axis ball screw linear motion stage, FUYU Motion) consisting of a stepper-motor (NEMA 23, STEPPERONLINE) controlled leadscrew which allowed for $400mm$ of vertical motion to $0.05mm$ position accuracy. A camera (GoPro HERO7) was mounted above the wing to capture kinematic trajectories (pitch angles) at 30 frames per second as shown in Figure 29 (a).

Vertical inflows were introduced by translating the flapping rig along a vertical rail with arbitrary upwards and downwards motions. As shown in Figure 29 (a), the flapping rig was supported by a vertical guide and wheel to stabilise the system during vertical motion.

4.2.2 Design and fabrication of wing and wing hinge

Considering a symmetric design of the wing and the hinge, the wing was constructed using two pieces of a rigid $1mm$ polystyrene plastic sheet covered by $0.0254mm$ thick aluminium and brass shims to control the wing mass with a total mass of 21.03 grams in air (3.77 grams under water) (see Figure 29 (b) and Table 6). In order to accommodate the F/T sensor, a rectangular cut out was included in the top corner of the wing as shown in Figure 29 (b). The ratio between the structural mass and added mass from the fluid, mass number, was considered as $M = m_w/\rho_f c^3$, where m_w is the mass of the wing (Ishihara et al., 2009b). The mass number was kept at $M = 0.17$ in this study, which is roughly 40 times smaller than that for an actual insect wing (Calliphora vicina $M = 6.4$) (Ennos, 1988a; Ishihara et al., 2014).

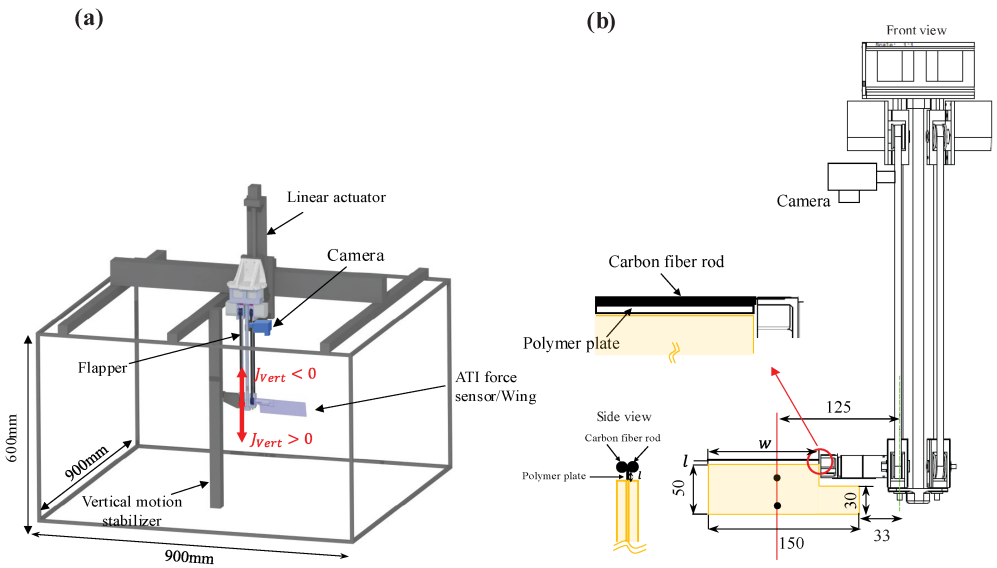

Figure 29: (a) Schematic illustration of the experimental setup. The wing and F/T sensor are mounted at the bottom of the rig opposite the guide connected to the vertical stabilizer for stability. The camera for capturing the whole wing motion is shown in its respective position. (b) Geometry and construction of the passive-pitching wing and hinge. Two marked points used for reconstruction of pitch angle are also shown on the wing. The hinge acts as a linear torsion spring whose stiffness is controlled by the elastic modulus of the material and the hinge dimensions. The axis of rotation being the vertical green dashed line and the wing radius of gyration R_{RoG} indicated by the vertical red dashed line. All dimensions are in mm.

Table 6: Properties and dimensions of wing and hinge

Experiment Property	**Value**
Wingspan (b)	$150mm$
Chord (c)	$51mm$
Wing thickness	$2.1mm$
Hinge length (l)	$1mm$
Hinge width (w)	$110mm$
Hinge thickness (t)	10,25, 50×10^{-6} m
Elastic modulus (E)	5.38×10^{9} Pa
Hinge stiffness (k)	4.93×10^{-5}, 7.7×10^{-4}, 6.2×10^{-3} $Nm \cdot rad^{-1}$

It is difficult to experimentally satisfy the mass number condition due to the limitation of available solid materials. This difference between the mass number of the model and that of the actual insect was also observed in prior experimental works (Ishihara et al., 2009b, 2014).

The wing hinge was constructed from a thin rectangular polymer plate (mylar sheet) clamped at both ends, similar in design to torsion springs used in other passive-pitching flapping robots (Ishihara et al., 2009b; Wood et al., 2013; Ishihara et al., 2014). The bottom end was sandwiched between two pieces of the wing and the top end was clamped by two $1mm$ diameter carbon fibre rods (see side view in Figure 29 (b)). The rods were connected to the F/T sensor via a 3D printed joint as shown in Figure 29 (b), and wing and hinge were joined using cyanoacrylate adhesive. Following Ishihara et al. (2009b), Whitney and Wood (2010) and Sum Wu et al. (2019), using Euler–Bernoulli beam theory which shows a linear relation between deflection angle and restoring torque in a clamped flat plate undergoing bending deformation, the torsional stiffness of the wing hinge was estimated by Equation 39.

$$k = \frac{Et^3 w}{12l} \tag{39}$$

where E is the elastic modulus and t, w and l are thickness, width, and length of the polymer plate, respectively (see Figure 29 (b) and Table 6). In this study, elastic wing hinges were created with stiffnesses ranging from 4.93×10^{-5} $Nm \cdot rad^{-1}$ to 6.2×10^{-3} $Nm \cdot rad^{-1}$ by variation in the polymer plate thickness.

4.2.3 Wing kinematics and test procedure

A sinusoidal flapping profile in a horizontal stroke plane, $\phi = 0.5\phi_{max}\cos(2\pi ft)$, with amplitude ϕ_{max} of 12° (measured from the aft-most position of the wing at the start of the forward stroke) was employed in this study (see Table 7 and Figure 30). Following Lentink and Dickinson (2009), Bhat et al. (2018), Jardin and Colonius (2018)) and Lyu et al. (2019) the velocity at the radius of gyration ($U_{RoG} = 2\phi_{max} f R_{RoG}$) was used as the reference velocity. Considering geometrically similar wings, when U_{RoG} is used to scale aerodynamic forces better convergence appears in the results in comparison to using velocity at the wing tip (Ishihara et al., 2014). This is of utmost importance when comparing results from various studies in the literature. A $Re = \rho_f U_{RoG} c/\mu$ of 3600 based on U_{RoG} and chord length was selected and kept constant in the present study (Table 7). The flapping amplitude and Reynolds number nominally match the flapping kinematics of bees (Bombus lapidarius $Re = 3700$) (Weis-Fogh,

Table 7: Experiment kinematics

Experiment Property	**Value**
Flapping frequency (f)	0.125 Hz
Flapping amplitude ($\phi_{\max}$)	120°
Radius of gyration ($R_{RoG} = \sqrt{I/S}$)	$125mm$
Reynolds number ($Re = \rho_f U_{RoG} c/\mu$)	3600
Fluid density (ρ_f)	1000 kg/m^3
Fluid viscosity (μ)	8.9×10^{-4} $N \cdot s/m^2$

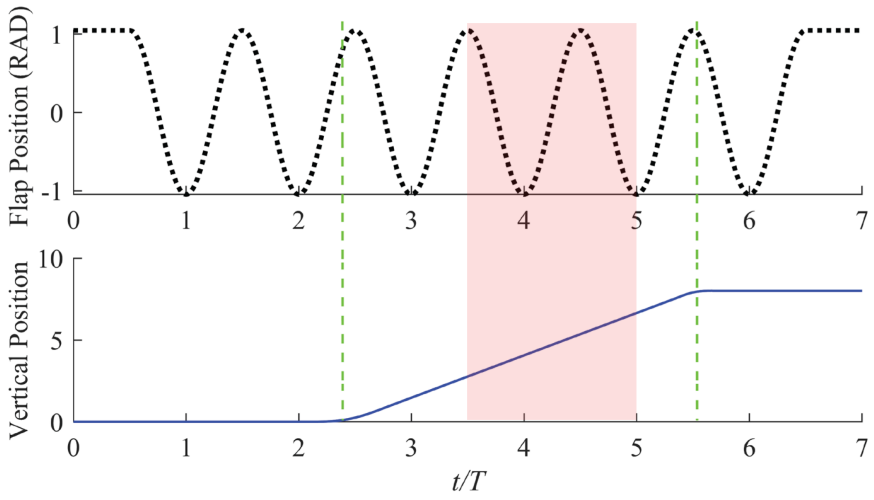

Figure 30: Flapping Kinematic Waveform. The flapping angle profile for an example test is shown here. The dashed line displays the sinusoidal flapping wave form, and the solid line shows the vertical flapper position normalized by chord length. T is the flapping period of the complete wing beat.

1973) and flies (Calliphora vicina $Re = 3400$) (Ennos, 1989). In this study the kinematics of forward and back strokes were symmetric.

Due to the high wingbeat frequencies of small size-scaled flapping wing flyers, it is likely that the majority of the perturbations encountered in realistic environments are likely to be of timescales much lower than those of the wingbeat. Thus, in this study the frequency of disturbance was assumed to be much larger than the wing flapping frequency and simulated as a uniform constant velocity perturbation in the freestream flow. The spatial extent of the disturbance would also likely be large in comparison to the size of the wing, thus a reasonable simulation of the disturbance can be obtained by plunging the wing at constant velocity in quiescent fluid.

Here we describe the experiment procedure followed for the upward oriented inflow perturbation, noting that the same procedure with opposite inflow direction was followed for downward inflow conditions. The wing was initially flapped in quiescent fluid (i.e. in pure hover), at a distance of 2 chord lengths from the free surface, at the top of the experiment tank, to minimise any surface effects. No disturbance of the water surface was observed. To intro-

duce an upwards inflow, the flapping rig was translated downwards over a distance of $400mm$ (8 chord lengths) with short acceleration and deceleration phases and constant velocity in between (dashed green lines in Figure 30). The duration of the acceleration and deceleration phases accounted for 1% of the entire duration of the inflow. Further details on the vertical position profile can be found in the supplementary material. To reduce both the transient effect from the acceleration phase at the start of the inflow, and any interference with the wake produced during initial pure hover before inflow onset, force measurements were commenced only after one complete stroke following the start of the inflow. Data was then collected for all subsequent strokes prior to commencement of the deceleration phase (red shading in Figure 30). The same procedure was employed for the downward inflow perturbations, with upwards translation of the rig from 2 chord lengths above the bottom of the tank, to approximately 2 chord lengths below the free surface.

The inflow ratio J_{Vert}, which is defined in Equation 40, was used to investigate the speed of vertical inflow.

$$J_{Vert} = \frac{U_{inflow}}{U_{RoG}} = \frac{U_{inflow}}{2\phi_{\max} f R_{RoG}} \tag{40}$$

$J_{Vert} < 0$ denotes downwards inflows and $J_{Vert} > 0$ denotes upwards inflows. The maximum range of inflow ratios analysed in this study was $J_{Vert} = \pm 0.6$. Relating this to flapping wing insects for bees and wasps which operate at approximately $Re = 3600$ (Weis-Fogh, 1973), $J_{Vert} = \pm 0.6$ indicates a wind velocity of approximately $3.12m/s$ (based on the wing tip velocity of these insects), comparable to the most likely atmospheric wind speeds in the first few meters from the Earth's surface (Watkins et al., 1995).

To compare the fluid dynamic force and the elastic reaction force of the hinge, the Cauchy number, Ch, was defined similar to prior works (Kolomenskiy et al., 2019; Ishihara et al., 2014) as shown in Equation 41.

$$Ch = \frac{4\rho_f \phi_{\max}^2 f^2 c^3 R_{RoG}^2}{k} \tag{41}$$

In this study three representative values of the Cauchy number $Ch = 0.09, 0.73 and 11.52$, spanning three orders of magnitude, were chosen (see Table 6, Table 7 and Equation 41). These represent wing hinges that can be classified as either stiff, moderate, or flexible, respectively.

4.2.4 Force measurement and data acquisition

Force measurements were made using an $ATINano - 17IP68$ force/torque (F/T) sensor mounted at the root of the wing. The sensor was connected to a signal conditioner and a PCI-6143 National Instruments DAQ Board linked to a PC. Data was processed using in-house developed code in MATLAB.

The F/T sensor measured forces in body-fixed coordinates x_L and y_L shown in Figure 31 (a). The raw force collected by the F/T sensor in body-fixed coordinate x_L comprised the inertial force from wing motion and the fluid mechanical force. Following prior works (Bhat et al., 2018; Nagai et al., 2009) the inertial force was measured by flapping the wing with the same test kinematics in air. Due to the considerably lower density of air compared to water the wing experienced negligible fluid mechanical forces, isolating the inertial force. The inertial force was phase averaged over 40 strokes to give an average inertial force in body-fixed coordinates for a single stroke. The fluid mechanical force in body-fixed coordinate x_L was isolated by removing inertia from the raw F/T sensor readings through Equation 42. The

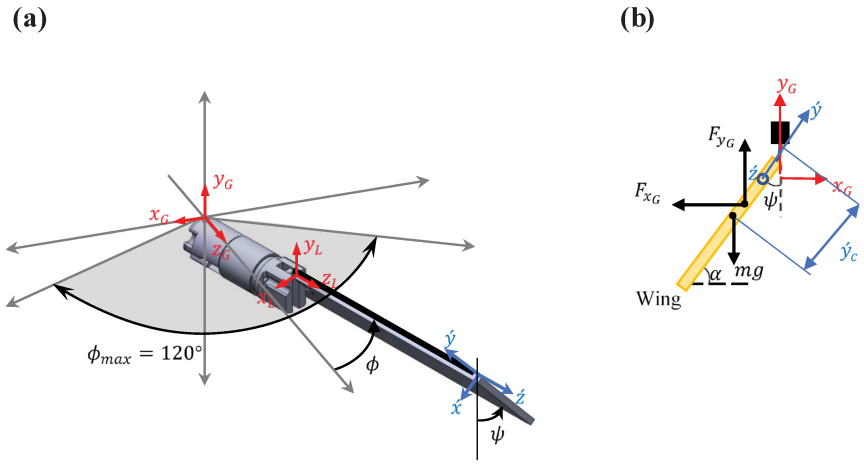

Figure 31: Coordinate Systems. (a) The body-fixed and global coordinate systems given the flapping angle ϕ and pitch angle with respect to vertical ψ. The $\acute{x}\acute{y}\acute{z}$-axes rotate with the flapping angle ϕ. (b) Side view of the wing showing lift F_{yG} and drag F_{xG} forces and the pitch angle α with respect to horizontal. $\acute{y}_c$ is the center of mass of the wing.

force component F_{x_G}) (drag) in global coordinate x_G (Figure 31 (a) and (b)) was calculated using the flapping position ϕ through Equations 43.

The force component F_{y_G} (lift) in global coordinate y_G (Figure 3 (b)) was obtained directly from the force measurements due to no acceleration in y_L and no rotation along the wingspan (z_L axis) (see Equation 44).

$$F_{x_L(\text{ fluid })} = F_{x_L(\text{ Sensor })} - F_{x_L(\text{ Inertia })} \tag{42}$$

$$F_{x_G} = F_{x_L(\text{ fluid })} \cos\phi \tag{43}$$

$$F_{y_G} = F_{y_L(\text{ fluid })} = F_{y_L(\text{ Sensor })} \tag{44}$$

The barometric pressure of the fluid during vertical motion had to be accounted for, however this was linearly proportional to depth and was removed by applying a correction which was calculated based on the maximum pressure difference over $400mm$ vertical translation, the instantaneous inflow velocity, and the corresponding depth to $F_{x_L,y_L(fluid)}$. The data was phase averaged over 20 strokes and filtered using a low-pass, 4^{th} order, Butterworth filter with a cut-off frequency of 8Hz which was significantly higher than the flapping frequency of the wing ($0.125Hz$)

For the selected kinematics and Reynolds number, the fluid mechanical forces were found to be symmetric for the forward and back strokes, and in the following analysis the results for both are considered together. Following Han et al. (2019), the instantaneous lift and drag coefficients C_L and C_D were calculated according to

$$C_L = \frac{2F_{y_G}}{\rho_f U_{RoG}^2 S}, \quad C_D = \frac{2F_{x_G}}{\rho_f U_{RoG}^2 S} \tag{45}$$

The surface area S of the wing was the total area of the wing excluding the cut out for the force sensor (Figure 29 (b)). The density of the fluid ρ_f was 1000 kg/m^3. Mean lift and

drag coefficients $\bar{C}_L$ and $\bar{C}_D$ were obtained by time-averaging the phase-averaged forces and indicate averages over a single stroke rather than the entire wing beat.

4.2.5 Wing Pitch Estimation

The wing motion was filmed using a camera recording 30 frames per second which was attached to the main shaft of the flapper rig at $400mm$ (8 chord lengths) above the wing (perpendicularly to the stroke plane), resulting in no relative velocity between wing and camera (see Figure 29). A stationary reference point on the ground of the experiment tank was used to identify wing's location in time within the wingbeat.

Spatial data of the wing were extracted from the recordings using DLTdv8; an open-source MATLAB-executed software which tracks positional information of two points marked on the wing (see Figure 29 (b)) via direct linear transformation (DLT) (Hedrick (2008)). These data were smoothed using a fourth order low-pass Butterworth filter with a cut-off frequency of $4Hz$. The pitch angle was calculated by projected distances between the points. We used the spatial data of a rigid wing performing prescribed pitching motion with the same geometry and marked points as the passive-pitching wing, and created a database consisting of angles and projected distances by pitching the rigid wing with different known angles and measurement of corresponding distances between the marked points via DLT. The pitch angle of the passive-pitching wing was computed using the measured inter-point distance and interpolating in the database. A similar method was used by Jakobi et al. (2018) and Kolomenskiy et al. (2019) to reconstruct wing kinematics of free flying bumblebees. Since the length of the polymer plate l is small there is no rotation along the x_L-axis, thus the pitch angle is assumed constant along the wingspan.

4.3 Results and discussion

4.3.1 Effects of Cauchy number on pitch angle

We defined the wing pitch angle with respect to the horizontal as $\alpha = \frac{\pi}{2} - \psi$ (Figure 31 (b)). Under quiescent conditions ($J_{Vert} = 0$), for all values of Ch, the pitching trajectory of the wing presented the maintenance of a high angle of attack during the translation phase of the stroke and the wing rotation during stroke reversal (black lines in Figure 32), as also noted by Ishihara et al. (2009b). Across the entire range of inflow ratios, the instantaneous angle of attack of the wing decreased with increasing the Cauchy number, as expected due to the reduction in wing hinge stiffness.

Under the effects of vertical inflows, the pitch angle exhibited two peaks before and after mid-stroke where the fluid mechanical moment dominates the pitch motion, especially for downward inflows (Figure 32). Comparison of the pitch angle in the different Ch revealed that the reduction in α was more apparent when the hinge stiffness changed from stiff ($Ch = 0.09$) to moderate ($Ch = 0.73$) particularly in the presence of upwards inflows (see Figure 32 (a) and (b)).

In general, the pitch angle α tended to decrease as the magnitude of inflow perturbation varies from $J_{Vert} = -0.6$ (downwards inflow) to $J_{Vert} = 0.6$ (upwards inflow). Within this range of inflow ratios, the pitch angle experienced the maximum reduction ($\Delta\alpha = 46.45°$) when the wing hinge was soft ($Ch = 11.52$) (see Table 3 and solid and dashed yellow lines in Figure 32 (b)). As shown in Figure 32 (a) (solid and dashed yellow lines) the minimum reduction

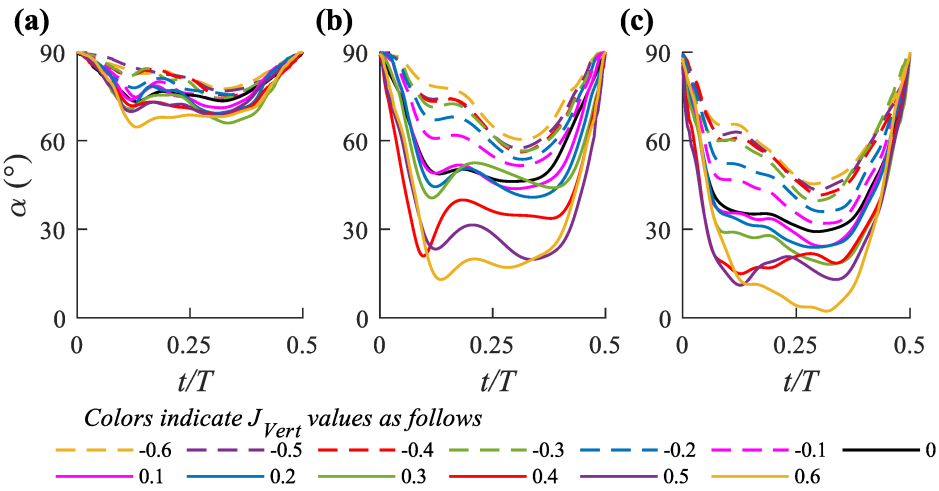

Figure 32: Instantaneous wing pitch angle α at (a) $Ch = 0.09$ (b) $Ch = 0.73$ (c) $Ch = 11.52$

Table 8: Reduction in the pitch angle at the mid-stroke between $J_{Vert} = -0.6$ and $J_{Vert} = 0.6, \Delta\alpha$. α_{mid} is the pitch angle at $t/T = 0.25$ in Figure 33.

Ch	$\Delta\alpha = \alpha_{\text{mid}_{-0.6}} - \alpha_{\text{mid}_{0.6}}(^\circ)$
0.09	11.87
0.73	43.48
11.52	46.45

in α occured for $Ch = 0.09$ ($\Delta\alpha = 11.87^\circ$) resulting from large hinge stiffness. For the wing with the moderate hinge stiffness ($Ch = 0.73$) the pitch angle reduction ($\Delta\alpha = 43.48^\circ$) in the presence of upwards and downwards perturbations was comparable to that measured in the case of $Ch = 11.52$ (Table 8 and Figure 32 (c)).

4.3.2 Time-resolved and mean lift and drag forces

To understand how the variation of the lift and drag coefficients (C_L and C_D) over the stroke were affected by inflow perturbations and the Cauchy number, the time-resolved measurements from the force sensor were examined. In general, the instantaneous drag of the wing displayed a nominally parabolic variation peaking at the mid-stroke (Figure 33 (a), (c) and (e)). This parabolic variation was also observed for time resolved C_L for downwards inflows reaching a peak slightly after the mid-stroke which corresponds to the main peak in the wing pitch angle during the stroke (Figure 33 (b), (d) and (f)). The variation in C_L over the stroke was consistent for the downwards inflows with proportional scaling down of forces when $|-J_{Vert}|$ increased. In contrast, a slight skew towards the end of the stroke in C_L was noted for upwards inflows after $J_{Vert} = 0.4$ which was more pronounced at the lower Cauchy numbers (Figure 33 (b) and (d)).

Comparison of the instantaneous lift and drag coefficients for different inflow ratios revealed that in all cases of Ch, the instantaneous lift coefficient was strongly affected by the inflow perturbations when the magnitude of inflow, J_{Vert}, varied from -0.6 to 0.6 while the sensitivity

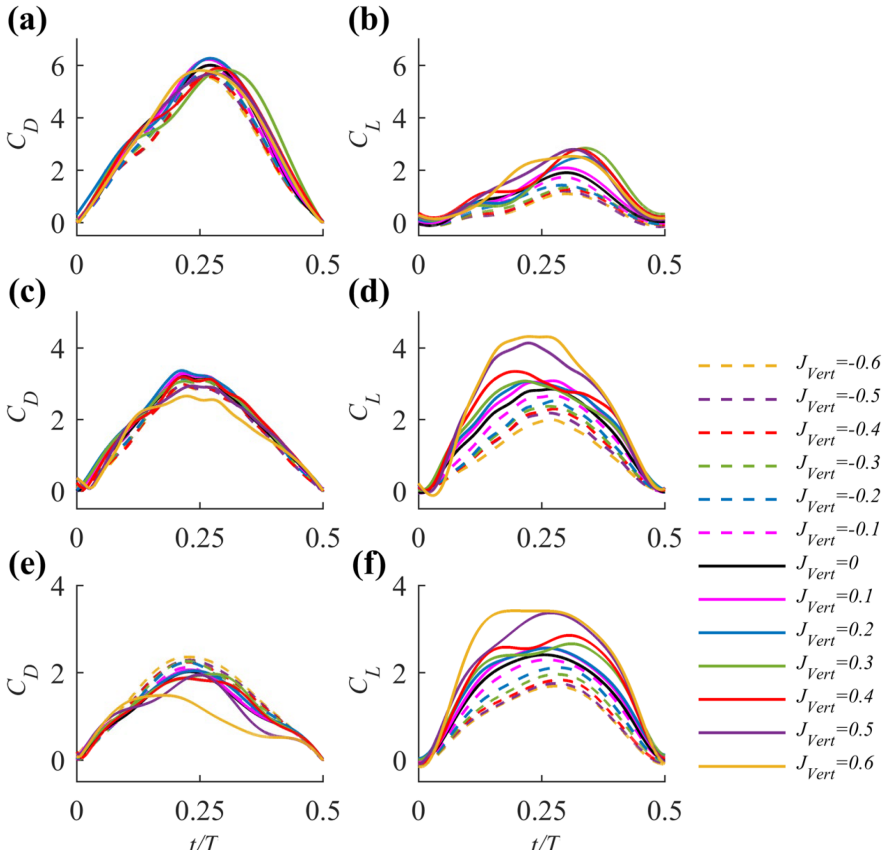

Figure 33: Instantaneous lift and drag coefficients C_L and C_D for upwards and downwards inflow perturbations at (a) and (b) $Ch = 0.09$. (c) and (d) $Ch = 0.73$. (e) and (f) $Ch = 11.52$

of the drag coefficient to the inflow ratio appeared to be less dramatic compared to C_L (see Figure 5). We compared the cycle-averaged coefficients of lift and drag, $\bar{C}_L$ and $\bar{C}_D$ under different inflow conditions to quantify the effects of the Cauchy number on the performance of the wings. In general the mean lift produced by the wing increased with increasing magnitude of upward inflow ($J_{Vert} > 0$) while the trend appeared to be in the reverse direction for downward inflows ($J_{Vert} < 0$). These trends were maintained for all Cauchy numbers (Figure 6 (a)).

The mean drag $\bar{C}_D$ exhibited three different trends with respect to the inflow ratio depending on the Cauchy number (Figure 6 (b)). $\bar{C}_D$ was almost independent to the inflow perturbations when the wing hinge had the moderate stiffness (Ch=0.73). $\bar{C}_D$ of the wing with a stiff hinge ($Ch = 0.09$) increased gradually when the magnitude of inflow perturbation varied from $J_{Vert} = -0.6$ to $J_{Vert} = 0.6$ while the opposite trend was observed for the wing with a soft hinge ($Ch = 11.52$), see Figure 6 (b). Compared to the prescribed pitching wing where an increase in $\bar{C}_D$ was noted by increasing the inflow ratio (Jones and Yamaleev, 2012, 2016), the passively pitching wing could adaptively change the wing pitch in response to inflow perturbations which resulted in the constant and decreasing $\bar{C}_D$ by increasing J_{Vert} of the intermediate and large Cauchy number.

Although the wing with the moderate hinge stiffness generated the greatest $\bar{C}_L$ in quiescent

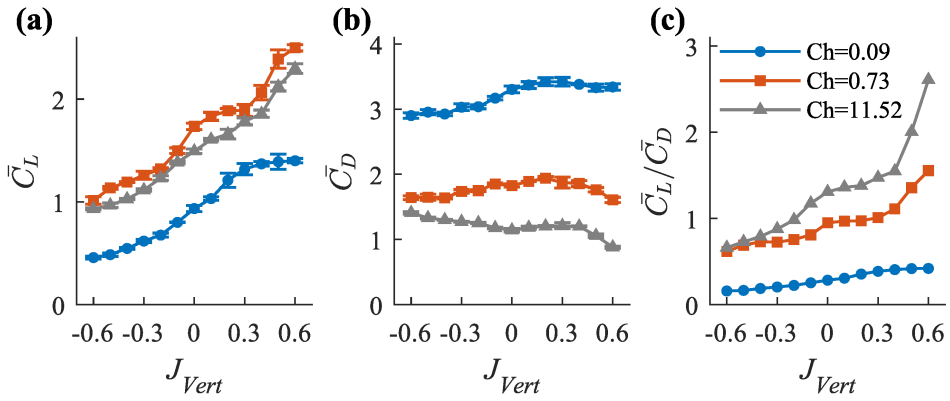

Figure 34: (a) Mean lift coefficient $\bar{C}_L$, (b) mean drag coefficient $\bar{C}_D$, (c) lift to drag ratio $\bar{C}_L/\bar{C}_D$ vs J_{Vert}.

condition ($J_{Vert} = 0$), the maximum lift to drag ratio ($\bar{C}_L/\bar{C}_D$), which can be interpreted as a measure of the wing performance, occurred at $Ch = 11.52$ (Figure 34 (c)). This indicates that the variation in $\bar{C}_D$ had more dominant effect on the wing performance. There was an increase in $\bar{C}_L/\bar{C}_D$ for upwards inflows as compared with that in the quiescent flow case which was more pronounced for the large Cauchy number. The constant or decreasing mean drag of the intermediate and large Cauchy number respectively could lead to decreasing input power to flap the wing (Wang, 2004), i.e. increasing wing performance for lift production. This observation is in contrast to the $\bar{C}_L/\bar{C}_D$ trend for prescribed pitching wing where increase in lift due to the effect of a vertical inflow perturbation came with an equivalent drag penalty leading to $\bar{C}_L/\bar{C}_D$ remained nearly unchanged in the presence of upwards inflows (Jones and Yamaleev, 2016; Ramamurti et al., 2004). Therefore, the wing performance of the passively pitching wing was more sensitive to the inflow perturbations compared to a prescribed pitching wing and it could be enhanced in the presence of the upwards inflows. However, the reduction in $\bar{C}_L/\bar{C}_D$ when the inflow ratio varied from 0 to -0.6 (Figure 34 (c)) indicates that the wing performance of the passively pitching wing was susceptible to the downwards inflows.

4.3.3 Inertial and external contributions of moments

For a thin wing with a flexural hinge in the absence of out-of-plane motion stems from the small length of the hinge used in this study, and by the perpendicular-axis theorem, the Euler equation describing rotation about the $\acute{z}$-axis (Figure 31 (a)) was simplified to Equation 46 similar to the approach adopted in (Whitney and Wood, 2010; Lei and Li, 2020; Li et al., 2018).

$$I_{\acute{z}\acute{z}}\ddot{\psi} = M_{\acute{z}} + I_{\acute{z}\acute{y}}\ddot{\phi}\cos\psi + \frac{1}{2}I_{\acute{z}\acute{z}}\dot{\phi}^2\sin 2\psi \tag{46}$$

where $I_{\acute{z}\acute{z}}$ and $I_{\acute{z}\acute{y}}$ are the elements from the matrix of the moment of inertia of the wing and $M_{\acute{z}}$ is the net externally applied moment about the $\acute{z}$-axis. $M_{\acute{z}}$ includes fluid mechanical moments (M_{fluid}), the elastic restoring moment ($M_{elastic} = -k\psi$) from the wing hinge, and the gravitational moment including buoyancy effects ($M_{gravity} = -mg\sin\psi\acute{y}_c$). The second term on the right-hand side of Equation 46 is the inertial moment, $M_{inertia}$, attributed to the fact

that the rotational axis does not pass through the center of mass of the wing ($\acute{y}_c$). Therefore, M_{fluid} is calculated according to

$$M_{\text{fluid}} = I_{\acute{z}\acute{z}}\ddot{\psi} + k\psi + mg\sin\psi\acute{y}_c - I_{\acute{z}\acute{y}}\ddot{\phi}\cos\psi - \frac{1}{2}I_{\acute{z}\acute{z}}\dot{\phi}^2\sin 2\psi \tag{47}$$

Lift and drag forces produced by the wing varied in concert with the fluid mechanical moments (M_{fluid}) achieved through a balance between the elastic restoring moment ($M_{elastic}$), gravitational moment ($M_{gravity}$) and inertial moment ($M_{inertia}$) at each instantaneous wing pitch angle. To better understand the significance of the variations in the fluid mechanical forces and the wing pitch angle, here we examined the proportion of each of these components under different inflow conditions and Cauchy numbers. All moment contributions were normalized by $\frac{1}{2}\rho U_{RoG}^2 Sc$ and represented as a moment coefficient C_M.

The inertial moment coefficient $C_{M_{inertia}}$ associated with the wing acceleration ($\ddot{\phi}$) was at a maximum when the wing position was at its point of reversal and reached zero at mid-stroke (Figure 35 (a1), (a2) and (a3)). Since the magnitude of this component was much smaller compared to the elastic and gravitational moments, the variations in $M_{inertia}$ have no significant effect on the wing kinematics, and therefore on the fluid mechanical moment. Across the entire range of inflow ratios, both $C_{M_{elastic}}$ and $C_{M_{fluid}}$ tended to decrease with increasing the Cauchy number (Figure 35 (c) and (d)). This reduction was more pronounced for the elastic moment which indicates that $M_{elastic}$ was more sensitive to the Cauchy number compared to the M_{fluid}. This means that the hinge stiffness played a more important role in the overall dynamics of force production. Moreover, $C_{M_{fluid}}$ scaled up when the inflow ratio varied from $J_{Vert} = -0.6$ to $J_Vert = 0.6$ which represents how the net force over the wing changes in the different conditions (Figure 35 (d)).

Comparison of $C_{M_{fluid}}$ and $C_{M_{elastic}}$ indicated the dominant component at each Cauchy number. For $Ch = 0.09$ where the gravitational moment had a minor contribution to $C_{M_{fluid}}$ due to the high pitch angle, the elastic moment offset the effects of fluid mechanical moment (see Figure 35 (b1), (c1) and (d1)). In contrast, the fluid mechanical moment coefficient $C_{M_{fluid}}$ dominated over $C_{M_{elastic}}$ for the wing with the soft hinge (Figure 35 (c3) and (d3)). At $Ch = 11.52$ the elastic moment was negligible resulting from the small stiffness, thereby balancing the fluid mechanical moment against gravitational moment (Figure 35 (b3) and (c3)). When the wing had the moderate stiffness ($Ch = 0.73$) the elastic moment was almost equal to the gravitational moment and half of the fluid mechanical moment (Figure 35 (b2), (c2) and (d2)). Although $C_{M_{fluid}}$ was greater than $C_{M_{elastic}}$ in this Cauchy number the difference between these two components was not as pronounced as that measured at $Ch = 11.52$.

4.3.4 Effects of inflow perturbations on net force

To assess the variation of the mean lift and drag coefficients with Ch versus the inflow ratio, contribution of the fluid force over the wing in the horizontal and vertical directions was investigated. The net fluid mechanical force was given by $F_{net} = \sqrt{\left(F_{x_G}^2 + F_{y_G}^2\right)}$ and non-dimensionally represented as the net force coefficient $C_{net} = \frac{2F_{net}}{\rho U_{RoG}^2 S}$. Calculating normal $\left(F_N = \frac{\left(F_{y_G}/\sin\alpha + F_{x_G}/\cos\alpha\right)}{(\cot\alpha + \tan\alpha)}\right)$ and tangential $\left(F_T = \frac{F_{x_G}}{\cos\alpha} - \frac{F_N}{\tan\alpha}\right)$ forces through measured lift and drag showed that across the entire range of inflow ratios the tangential forces were negligible in comparison with normal forces meaning the net force was nearly normal to the

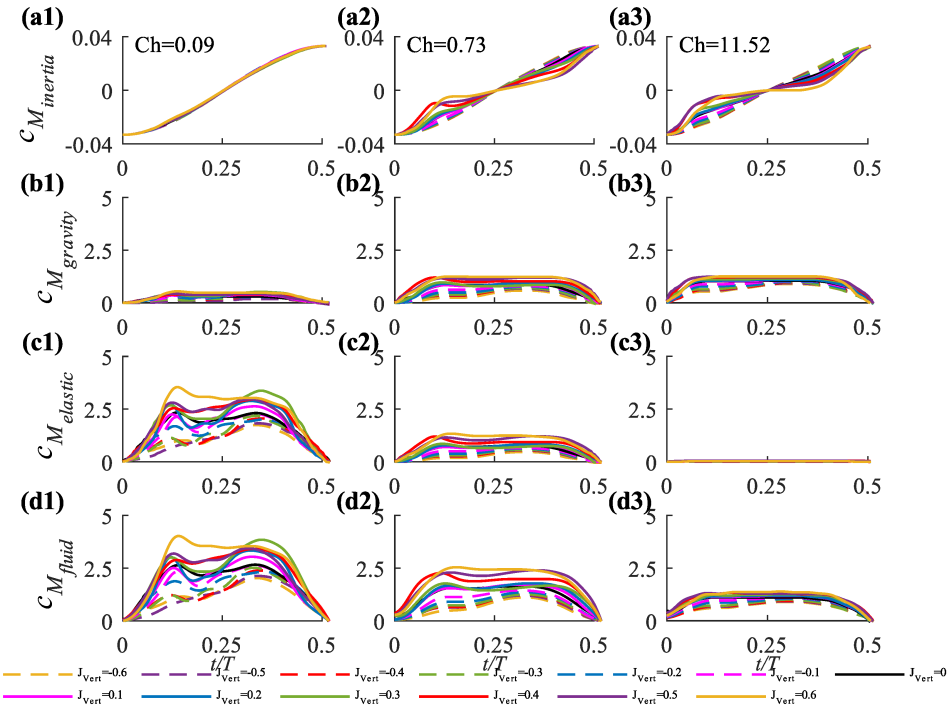

Figure 35: Instantaneous moment coefficients, non-dimensionalised by $\frac{1}{2}\rho U_{RoG}^2 Sc$. (a) Inertial $C_{M_{inertia}}$. (b) Gravitational $C_{M_{gravity}}$. (c) Elastic restoring $C_{M_{elastic}}$. (d) Fluid mechanical $C_{M_{fluid}}$ at $Ch = 0.09$. (a1, b1, c1, d1), $Ch = 0.73$ (a2, b2, c2, d2) and $Ch = 11.52$ (a3, b3, c3, d3). All figures show the absolute values of the moments.

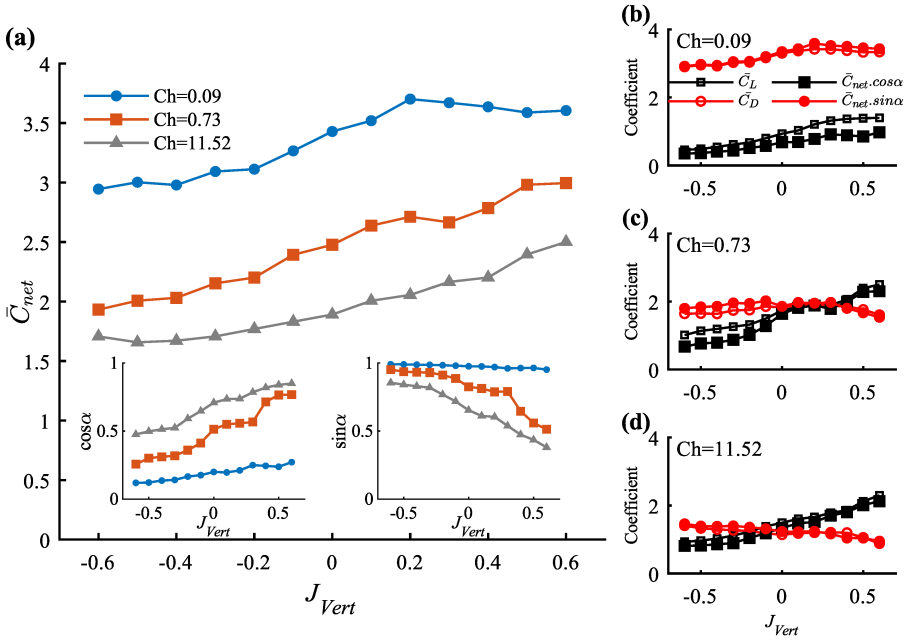

Figure 36: (a) Mean net force coefficient $\bar{C}_{net}$. Horizontal and vertical components of the net force $\bar{C}_{net} \cdot \sin\alpha$ and $\bar{C}_{net} \cdot \cos\alpha$ as well as measured mean lift and drag coefficients $\bar{C}_L$ and $\bar{C}_D$ at (b) $Ch = 0.09$. (c) $Ch = 0.73$. (d) $Ch = 11.52$. The insets in (a) show the cycle-averaged $\sin\alpha$ and $\cos\alpha$ for different Cauchy numbers.

wing. The coefficient $\bar{C}_{net}$ was obtained by time-averaging the phase-averaged force over 12 strokes. In general, the $\bar{C}_{net}$ over the wing increased with increasing magnitude of upward inflow ($J_{Vert} > 0$) while the opposite trend was observed for downward inflows ($J_{Vert} < 0$) for all cases of Ch (Figure 36 (a)). This observation aligns with the findings for the fluid mechanical moment M_{fluid} shown in Figure 35 (d). The net force can be decomposed into the vertical and horizontal components based on the pitch angle time history (via $\cos\alpha(t)$ and $\sin\alpha(t)$, respectively). As the inflow ratio increased from $J_{Vert} = -0.6$ to 0.6 the passively pitching wing adaptively changed the wing pitch such that its pitch angle tended to decrease (Figure 4). This reduction had a beneficial effect on growing the vertical component of the net force (via increasing $\cos\alpha(t)$ shown as inset in Figure 36 (a)) whereas it was a counter to increasing the magnitude of the horizontal component (via reduction in $\sin\alpha(t)$, see inset in Figure 36 (a)). Thus, variations of the vertical and horizontal components of the net force versus the inflow ratio depended on the variations in $\bar{C}_{net}$ and α.

Evolutions of $\bar{C}_L$ against the inflow ratio can be represented by variations of the vertical component of the net force ($\bar{C}_L \cdot \cos\alpha$). For all values of Ch used in this study, increase in $\bar{C}_{net}$ and reduction in α had a complementary effect on growing the vertical force component as J_{Vert} changed from -0.6 to 0.6 (Figure 36 (a)) which resulted in a rising trend in the mean lift $\bar{C}_L$ (Figure 36 (b), (c) and (d)).

The horizontal component of the net force ($\bar{C}_{net} \cdot \sin\alpha$) was used to explore the effects of Ch on variations in $\bar{C}_D$ with respect to the inflow ratio. Since increase in $\bar{C}_{net}$ and reduction in α

had contrary effects on the magnitude of the horizontal component of the net force (see Figure 36 (a)), three different trends in this force component occurred for $-0.6 \leq J_{Vert} \leq 0.6$. These trends depended on the competition between the beneficial effect of $\bar{C}_{net}$ and the detrimental influence of α at different Cauchy numbers. At $Ch = 0.09$ since the elastic moment $M_{elastic}$ was remarkably large the variation in the pitch angle was limited. As a result, the increase in $\bar{C}_{net}$ was superior to the adverse effect of the reduction in α leading to the increasing trend in the mean drag for $-0.6 \leq J_Vert \leq 0.6$ (see Figure 36 (b)). For $Ch = 0.73$, the adverse effect of the reduction in α offset the beneficial effect of the increase in $\bar{C}_{net}$ on growing the horizontal force component. This was due to the moderate elastic moment $M_{elastic}$ which was comparable with the fluid mechanical moment M_{fluid} (see Figure 35 (c2) and (d2)), causing the mean drag remained approximately constant with respect to the inflow ratio (Figure 36 (b)). For a wing with the soft hinge ($Ch = 11.52$) the negligible elastic moment $M_{elastic}$ caused the large variation in the pitch angle. Consequently, the detrimental effect of the reduction in α dominated over the increase in $\bar{C}_{net}$ resulting in a decreasing trend in the mean drag when the inflow ratio varies from $J_{Vert} = -0.6$ to 0.6 (see Figure 36 (b)).

4.4 Conclusion

The performance of a passive-pitching flapping wing under a uniform vertical inflow perturbation (perpendicular to the stroke plane) was studied experimentally using a Reynolds-scaled flapping wing apparatus at Reynolds number of 3600. The stiffness of the hinge was characterized by the Cauchy number (Ch) that represents the ratio between the fluid dynamic and the elastic reaction forces, was changed from 0.09 (stiff hinge) to 0.73 (moderate hinge) and 11.52 (soft hinge) in this study. The overall lift and drag forces over the wing were measured by a F/T sensor and the instantaneous pitch angle of the wing (α) was captured using a camera. The magnitudes of the inflow perturbation, represented as a ratio of the vertical flow velocity, due to the perturbation, to the wing velocity, was varied from $J_{Vert} = -0.6$ (downwards inflow) to $J_{Vert} = 0.6$ (upwards inflow).

Compared to quiescent conditions ($J_{Vert=0}$), the mean drag ($\bar{C}_D$) altered from an increasing to a decreasing trend as Ch was changed from 0.09 to 11.52 with increasing the magnitude of the upward inflows. While the mean lift ($\bar{C}_L$) was found to increase with increasing inflow ratio, irrespective to the Cauchy number. According to the kinematics measurement, the passively pitching wing adaptively decreased the pitch angle in response to the upwards inflows. This reduction in α was more apparent for the large Cauchy number (soft hinge).

Analysis of the moments due to aerodynamic, elastic, and gravitational forces revealed that the reduction in the wing pitch was mainly determined by the elastic moment. This reduction was accompanied with the increase in the fluid mechanical moment which had a complementary effect on the lift force leading to rising trend in $\bar{C}_L$L and a contrary influence on drag resulting in appearing three different trends in $\bar{C}_D$. The effect of the reduction in wing pitch tended to be from minor to dominant in comparison to the effect of the increase in the fluid mechanical moment as Ch was changed from 0.09 to 11.52.

All trends observed for the pitching angle, $\bar{C}_L$, $\bar{C}_D$, and the fluid mechanical moment in upwards inflows were found to be opposite in the presence of the downwards inflows as $|-J_{Vert}|$ increased.

These results highlight the complex interactions between passively pitching flapping wings and freestream perturbations and will guide the design of miniature flying crafts with such

architectures. Future work in this area could focus on flapping wing performing both passive pitching and flapping motions which may lead to a simpler actuation system.

References

Altshuler, D.L., Dickson, W.B., Vance, J.T., Roberts, S.P., Dickinson, M.H., 2005. Short-amplitude high-frequency wing strokes determine the aerodynamics of honeybee flight. Proceedings of the National Academy of Sciences 102, 18213–18218.

Beatus, T., Cohen, I., 2015. Wing-pitch modulation in maneuvering fruit flies is explained by an interplay between aerodynamics and a torsional spring. Physical Review E 92, 022712.

Bergou, A.J., Ristroph, L., Guckenheimer, J., Cohen, I., Wang, Z.J., 2010. Fruit flies modulate passive wing pitching to generate in-flight turns. Physical review letters 104, 148101.

Bergou, A.J., Xu, S., Wang, Z.J., 2007. Passive wing pitch reversal in insect flight. Journal of Fluid Mechanics 591, 321–337.

Bhat, S.S., Zhao, J., Sheridan, J., Hourigan, K., Thompson, M.C., 2018. The leading-edge vortex on a rotating wing changes markedly beyond a certain central body size. Royal Society open science 5, 172197.

Birch, J.M., Dickinson, M.H., 2003. The influence of wing–wake interactions on the production of aerodynamic forces in flapping flight. Journal of experimental biology 206, 2257–2272.

Birch, J.M., Dickson, W.B., Dickinson, M.H., 2004. Force production and flow structure of the leading edge vortex on flapping wings at high and low reynolds numbers. Journal of Experimental Biology 207, 1063–1072.

Bode-Oke, A.T., Zeyghami, S., Dong, H., 2018. Flying in reverse: kinematics and aerodynamics of a dragonfly in backward free flight. Journal of The Royal Society Interface 15, 20180102.

Dai, H., Luo, H., Doyle, J.F., 2012. Dynamic pitching of an elastic rectangular wing in hovering motion. Journal of Fluid Mechanics 693, 473–499.

D'Humieres, D., Ginzburg, I., Krafczyk, M., Lallemand, P., Luo, L.S., 2002. Multiple-relaxation-time lattice Boltzmann models in three dimensions. The Royal Society 360, 437–451.

Dickinson, M.H., Lehmann, F.O., Sane, S.P., 1999. Wing rotation and the aerodynamic basis of insect flight. Science 284, 1954–1960.

Ellington, C.P., 1984. The aerodynamics of hovering insect flight. i. the quasi-steady analysis. Philosophical Transactions of the Royal Society of London. B, Biological Sciences 305, 1–15.

Ellington, C.P., Van Den Berg, C., Willmott, A.P., Thomas, A.L., 1996. Leading-edge vortices in insect flight. Nature 384, 626–630.

Ennos, A.R., 1987. A comparative study of the flight mechanism of diptera. Journal of Experimental Biology 127, 355–372.

Ennos, A.R., 1988a. The importance of torsion in the design of insect wings. Journal of experimental Biology 140, 137–160.

Ennos, A.R., 1988b. The inertial cause of wing rotation in diptera. Journal of experimental biology 140, 161–169.

Ennos, A.R., 1989. The effect of size on the optimal shapes of gliding insects and seeds. Journal of Zoology 219, 61–69.

Farrell Helbling, E., Wood, R.J., 2018. A review of propulsion, power, and control architectures for insect-scale flapping-wing vehicles. Applied Mechanics Reviews 70.

Guo, Z.L., Zheng, C.G., Shi, B.C., 2002. Non-equilibrium extrapolation method for velocity and pressure boundary conditions in the lattice Boltzmann method. Chinese physics 11, 366–374.

Han, J.S., Nguyen, A.T., Han, J.H., 2019. Aerodynamic characteristics of flapping wings under steady lateral inflow. Journal of Fluid Mechanics 870, 735–759.

Hao, J., Wu, J., Zhang, Y., 2019. Aerodynamic performance of a passive pitching model on bionic flapping wing micro air vehicles. Applied bionics and biomechanics 2019.

Hedrick, T.L., 2008. Software techniques for two-and three-dimensional kinematic measurements of biological and biomimetic systems. Bioinspiration & biomimetics 3, 034001.

Huang, Q., Mazharmanesh, S., Tian, F.B., Young, J., Lai, J., Ravi, S., 2021. CFD solver validations for simulating passively pitching tandem wings in hovering flight. The 24th International Congress on Modelling and Simulation (MODSIM2021) .

Huang, Q., Tian, F.B., Young, J., Lai, J.C.S., 2020a. A diffused interface immersed boundary–lattice Boltzmann method for simulation of channel flow. 22nd Australasian Fluid Mechanics Conference AFMC2020, 7-10 December 2020, Brisbane, Australia .

Huang, Q., Tian, F.B., Young, J., Lai, J.C.S., 2021a. Transion to chaos in a two-sided collapsible channel flow. Journal of Fluid Mechanics 926.

Huang, Q., Wang, L., Tian, F.B., Young, J., Lai, J.C.S., 2021b. A diffused interface immersed boundary–lattice boltzmann method for simulation of stenosis. 14th World Congress on Computational Mechanics & ECCOMAS Congress 2021, 11-15 January 2021, Paris France .

Ishihara, D., 2018. Role of fluid-structure interaction in generating the characteristic tip path of a flapping flexible wing. Physical Review E 98, 032411.

Ishihara, D., Horie, T., 2016. Passive mechanism of pitch recoil in flapping insect wings. Bioinspiration & biomimetics 12, 016008.

Ishihara, D., Horie, T., Denda, M., 2009a. A two-dimensional computational study on the fluid–structure interaction cause of wing pitch changes in dipteran flapping flight. Journal of Experimental Biology 212, 1–10.

Ishihara, D., Horie, T., Niho, T., 2014. An experimental and three-dimensional computational study on the aerodynamic contribution to the passive pitching motion of flapping wings in hovering flies. Bioinspiration & biomimetics 9, 046009.

Ishihara, D., Yamashita, Y., Horie, T., Yoshida, S., Niho, T., 2009b. Passive maintenance of high angle of attack and its lift generation during flapping translation in crane fly wing. Journal of Experimental Biology 212, 3882–3891.

Jakobi, T., Kolomenskiy, D., Ikeda, T., Watkins, S., Fisher, A., Liu, H., Ravi, S., 2018. Bees with attitude: the effects of directed gusts on flight trajectories. Biology open 7, bio034074.

James, J., Iyer, V., Chukewad, Y., Gollakota, S., Fuller, S.B., 2018. Liftoff of a 190 mg laser-powered aerial vehicle: The lightest wireless robot to fly, in: 2018 IEEE International Conference on Robotics and Automation (ICRA), IEEE. pp. 3587–3594.

Jardin, T., Colonius, T., 2018. On the lift-optimal aspect ratio of a revolving wing at low reynolds number. Journal of The Royal Society Interface 15, 20170933.

Jones, M., Yamaleev, N., 2012. The effect of a gust on the flapping wing performance, in: 50th AIAA Aerospace Sciences Meeting including the New Horizons Forum and Aerospace Exposition, p. 1080.

Jones, M., Yamaleev, N.K., 2016. Effect of lateral, downward, and frontal gusts on flapping wing performance. Computers & Fluids 140, 175–190.

Kolomenskiy, D., Ravi, S., Xu, R., Ueyama, K., Jakobi, T., Engels, T., Nakata, T., Sesterhenn, J., Schneider, K., Onishi, R., et al., 2019. The dynamics of passive feathering rotation in hovering flight of bumblebees. Journal of Fluids and Structures 91, 102628.

Krüger, T., Kusumaatmaja, H., Kuzmin, A., Shardt, O., Silva, G., Viggen, E.M., 2017. The lattice Boltzmann method. Springer International Publishing, Switzerland.

Lallemand, P., Luo, L.S., 2000. Theory of the lattice Boltzmann method: Dispersion, dissipation, isotropy, Galilean invariance, and stability. Physical Review E - Statistical Physics, Plasmas, Fluids, and Related Interdisciplinary Topics 61, 6546–6562.

Lee, C., Su, Z., Zhong, H., Chen, S., Zhou, M., Wu, J., 2013. Experimental investigation of freely falling thin disks. part 2. transition of three-dimensional motion from zigzag to spiral. Journal of Fluid Mechanics 732, 77–104.

Lei, M., Li, C., 2020. The aerodynamic performance of passive wing pitch in hovering flight. Physics of Fluids 32, 051902.

Lentink, D., Dickinson, M.H., 2009. Biofluiddynamic scaling of flapping, spinning and translating fins and wings. Journal of Experimental Biology 212, 2691–2704.

Li, Z., Suntharasantic, S., Bai, S., Chirarattananon, P., 2018. Aeromechanic models for flapping-wing robots with passive hinges in the presence of frontal winds. IEEE Access 6, 53890–53906.

Liu, H., Ravi, S., Kolomenskiy, D., Tanaka, H., 2016. Biomechanics and biomimetics in insect-inspired flight systems. Philosophical Transactions of the Royal Society B: Biological Sciences 371, 20150390.

Luo, H., Tian, F.B., Lu, X.Y., 2010. Effect of mass ratio for a flexible flapping wing during forward flight, in: APS Division of Fluid Dynamics Meeting Abstracts, pp. GT–004.

Luo, L.S., Liao, W., Chen, X., Peng, Y., Zhang, W., 2011. Numerics of the lattice Boltzmann method: Effects of collision models on the lattice Boltzmann simulations. Physical Review E 83, 1–24.

Lynch, J., Gau, J., Sponberg, S., Gravish, N., 2021. Dimensional analysis of spring-wing systems reveals performance metrics for resonant flapping-wing flight. Journal of the Royal Society Interface 18, 20200888.

Lyu, Y.Z., Zhu, H.J., Sun, M., 2019. Aerodynamic forces and vortical structures of a flapping wing at very low reynolds numbers. Physics of Fluids 31, 041901.

Mazharmanesh, S., Stallard, J., Medina, A., Fisher, A.M., Ando, N., Tian, F., Young, J., Ravi, S., 2021. Performance of passively pitching flapping wings in the presence of vertical inflows. Bioinspiration & Biomimetics .

Mohamed, A., White, C., Watkins, S., 2012. A numerical study of the updrafts over a building, with comparison to wind-tunnel results, in: 15th Australasian Wind Engineering Society Workshop. Sydney, Australia, pp. 23–24.

Moore, M.N.J., 2015. Torsional spring is the optimal flexibility arrangement for thrust production of a flapping wing. Physics of Fluids 27, 091701.

Nagai, H., Isogai, K., Fujimoto, T., Hayase, T., 2009. Experimental and numerical study of forward flight aerodynamics of insect flapping wing. AIAA journal 47, 730–742.

Norberg, R.Å., 1972. The pterostigma of insect wings an inertial regulator of wing pitch. Journal of comparative physiology 81, 9–22.

Norberg, R.Å., 1975. Hovering flight of the dragonfly aeschna juncea l., kinematics and aerodynamics, in: Swimming and flying in nature. Springer, pp. 763–781.

Peskin, C.S., 2002. The immersed boundary method. Acta Numerica 11, 479–517.

Platzer, M.F., Jones, K.D., Young, J., Lai, J.C., 2008. Flapping wing aerodynamics: progress and challenges. AIAA journal 46, 2136–2149.

Ramamurti, R., Sandberg, W., Lohner, R., 2004. The influence of fin rigidity and gusts on the force production in fishes and insects: A computational study, in: 42nd AIAA Aerospace Sciences Meeting and Exhibit, p. 404.

Shahzad, A., Tian, F.B., Young, J., Lai, J.C., 2016. Effects of wing shape, aspect ratio and deviation angle on aerodynamic performance of flapping wings in hover. Physics of Fluids 28, 111901.

Shyy, W., Aono, H., Chimakurthi, S.K., Trizila, P., Kang, C.K., Cesnik, C.E., Liu, H., 2010. Recent progress in flapping wing aerodynamics and aeroelasticity. Progress in Aerospace Sciences 46, 284–327.

Sum Wu, K., Nowak, J., Breuer, K.S., 2019. Scaling of the performance of insect-inspired passive-pitching flapping wings. Journal of the Royal Society Interface 16, 20190609.

Sun, M., Lan, S.L., 2004. A computational study of the aerodynamic forces and power requirements of dragonfly (aeschna juncea) hovering. Journal of Experimental Biology 207, 1887–1901.

Wang, Z.J., 2004. The role of drag in insect hovering. Journal of Experimental Biology 207, 4147–4155.

Wang, Z.J., 2005. Dissecting insect flight. Annu. Rev. Fluid Mech. 37, 183–210.

Wang, Z.J., Russell, D., 2007. Effect of forewing and hindwing interactions on aerodynamic forces and power in hovering dragonfly flight. Physical review letters 99, 148101.

Watkins, S., Saunders, J., Hoffmann, P., 1995. Turbulence experienced by moving vehicles. part i. introduction and turbulence intensity. Journal of Wind Engineering and Industrial Aerodynamics 57, 1–17.

Weis-Fogh, T., 1973. Quick estimates of flight fitness in hovering animals, including novel mechanisms for lift production. Journal of experimental Biology 59, 169–230.

Whitney, J.P., Wood, R.J., 2010. Aeromechanics of passive rotation in flapping flight. Journal of fluid mechanics 660, 197–220.

Wood, R., Nagpal, R., Wei, G.Y., 2013. Flight of the robobees. Scientific American 308, 60–65.

Yu, D., Mei, R., Shyy, W., 2002. A multi-block lattice boltzmann method for viscous fluid flows. International journal for numerical methods in fluids 39, 99–120.

5 Performance Metric

5.1 Peer-reviewed Journal and Conference Papers

1. Mazharmanesh, S., Stallard, J., Medina, A., Fisher, A., Ando, N., Tian, F.B., Young, J. and Ravi, S., 2021. Effects of uniform vertical inflow perturbations on the performance of flapping wings. Royal Society Open Science, 8(6), p.210471.

2. Li, L., Ravi, S., Xie, G. and Couzin, ID., 2021. Using a robotic platform to study the influence of relative tailbeat phase on the energetic costs of side-by-side swimming in fish. Proceedings of the Royal Society A, 2249(477)

3. Mazharmanesh, S., Stallard, J., Medina, A., Fisher, A.M., Ando, N., Tian, F., Young, J. and Ravi, S., 2021. Performance of passively pitching flapping wings in the presence of vertical inflows. Bioinspiration & Biomimetics.

4. Huang, Q., Mazharmanesh, S., Tian, F.-B., Young, J., Lai, J., and Ravi, S., "CFD solver validations for simulating passively pitching tandem wings in hovering flight," The 24th International Congress on Modelling and Simulation (MODSIM2021),2021.

5. Huang, Q., Wang, L., Ravi, S., Tian, F.-B., Young, J. and Lai, J.C.S., 2021. Benchmarking a coupled finite element-immersed boundary-lattice Boltzmann method solver for simulations of collapsible tube flows, 5th Australasian Conference on Computational Mechanics

6. Yeo, E.C., Huang, Q., 2021. Numerical study of passively pitching flapping wings in hovering flight, AIAA Region VII Student Conference

7. Huang, Q., Liu, Z., Ravi, S., Tian, F.-B., Young, J. and Lai, J.C.S., 2021. Reducing velocity error and its consequences by an iterative feedbackimmersed boundary method, 15th World Congress on Computational Mechanic and 8th Asian Pacific Congress on Computational Mechanics

8. Huang, Q., Moni, A., Liu, Z., Ravi, S., Tian, F.-B., Young, J. and Lai, J.C.S., 2021. Streamline penetration, velocity error and consequences of the feedback immersed boundary method (prepared to submit)

5.2 Theses

1. Yeo, E.C. Numerical study of passively pitching flapping wings in hovering flight, Undergraduate thesis, Bachelors of Aerospace Engineering, UNSW-Canberra, 2020

2. Rory, D. Experimental analysis of the performance of passively pitching flapping wing, Undergraduate thesis, Bachelors of Aerospace Engineering, UNSW-Canberra, 2021

5.3 Awards and media exposure

5.4 Students support